A Reproduced Copy

OF

DRA

NASA CONTRACTOR REPORT 166561

NUMERICAL SOLUTION OF THREE-DIMENSIONAL UNSTEADY TRANSONIC FLOW OVER WINGS INCLUDING INVISCID/VISCOUS INTERACTIONS

D. P. Rizzetta and C. J. Borland

CONTRACT NAS2- 10762
February, 1984

NASA

NASA CONTRACTOR REPORT 166561

NUMERICAL SOLUTION OF THREE-DIMENSIONAL UNSTEADY TRANSONIC FLOW OVER WINGS INCLUDING VISCID/VISCOUS INTERACTIONS

D. P. Rizzetta and C. J. Borland
Boeing Military Airplane Company
Seattle, Washington

Prepared for
Ames Research Center
under Contract NAS2-10762

National Aeronautics and
Space Administration

Ames Research Center
Moffett Field, California 94035

NUMERICAL SOLUTION OF THREE-DIMENSIONAL UNSTEADY TRANSONIC FLOW OVER WINGS INCLUDING INVISCID/VISCOUS INTERACTIONS

D. P. Rizzetta and C. J. Borland
Boeing Military Airplane Company
Seattle, Washington

Abstract

A numerical procedure is presented for computing the unsteady transonic flowfield about three-dimensional swept wings undergoing general time dependent motions. The outer inviscid portion of the flow is assumed to be governed by the modified unsteady transonic small disturbance potential equation which is integrated in the time domain by means of an efficient alternating direction implicit approximate factorization algorithm. Gross dominant effects of the shock-boundary-layer interaction are accounted for by a simple empirically defined model. Viscous flow regions adjacent to the wing surface and in the trailing wake are described by a set of integral equations appropriate for compressible turbulent shear layers. The two-dimensional boundary-layer equations are applied quasi-statically stripwise across the span. Coupling with the outer inviscid flow is implemented through use of the displacement thickness concept within the limitations of small disturbance theory. Validity of the assumptions underlying the method is established by comparison with experimental data for the flow about a high aspect ratio transport wing having an advanced airfoil section.

Draft Report received August, 1982, Revised Final Report received November, 1983.

TABLE OF CONTENTS

NOMENCLATURE

a	$= (\frac{E}{c}) + 2\ G_S\ \xi_y\ \phi_\eta$
A	$= \varepsilon_1 M_\infty^2\ k^2$
AR	= aspect ratio
b	$= (\frac{F}{c^2}) + G_S\ \xi_y^2$
B	$= 2\ M_\infty^2\ k$
c	= local section chord nondimensionalized by c_r (c_s/c_r).
c_r	= reference chord
c_s	= local section chord
C_E	= entrainment coefficient $(\frac{1}{\rho_e U_e} \frac{d}{dS} \int_o^\delta \rho U\ dN)$
C_f	= skin friction coefficient (see Eq. A-11)
C_l	= total wing lift coefficient $(2 \int_o^{\eta_{tip}} \int_o^1 (C_p^- - C_p^+) d\xi d\eta)$
C_m	= total wing moment coefficient, moment taken about leading edge of root section
C_p	= local section pressure coefficient
C_τ	= see Eq. A-16
$(C_\tau)_{EQ_o}$	= see Eq. A-20
$\frac{d\bar{H}}{dH_1}$	= see Eq. A-13
D_ξ, D_η	= type-dependent finite difference operators

E = $1 - M_\infty^2$

f = local instantaneous surface section definition ($z = f(x,t)$)

f_{R_ξ} = local viscous ramp surface slope modification

F = $-1/2\ (\gamma + 1)\ M_\infty^2$

F_A = see Eq. A-15

F_1 = see Eq. 24

F_2 = see Eq. 25

g = initial ϕ distribution, $\phi(\xi, \eta, \zeta, 0)$

G = $1/2\ (\gamma - 3)\ M_\infty^2$

G_S = $1 - M_\infty^2$

G_N = $1/2\ (\gamma - 1)\ M_\infty^2 - 1$

h = initial ϕ_t distribution, $\phi_t\ (\xi, \eta, \zeta, 0)$

H = $-(\gamma - 1)\ M_\infty^2$

H_0 = shape factor, $\frac{\delta^*}{\theta}$

H_1 = see Eq. A-14

$\overline{H}$ = shape parameter, $\frac{1}{\theta} \int_0^\infty \frac{\rho}{\rho_e} \left(1 - \frac{U}{U_e}\right) dN$

k = nondimensional time scaling

k_c = reduced frequency, $\frac{\omega c_r}{U_\infty}$

M = Mach number

N = physical normal boundary-layer coordinate

Pr_t = turbulent Prandtl number

r = adiabatic recovery factor, $(Pr_t)^{1/3}$

Re_∞ = freestream Reynolds number based upon chord, $\frac{\rho_\infty U_\infty c_r}{\mu_\infty}$

Re_θ = momentum defect thickness Reynolds number, $\frac{\rho_e U_e \theta}{\mu_e}$

S = physical streamwise boundary-layer coordinate

S_0 = Sutherland law gas constant

t = physical time nondimensionalized by $\frac{c_r}{k U_\infty}$

T = temperature

U = streamwise velocity component

x = physical streamwise coordinate nondimensionalized by c_r

y = physical spanwise coordinate nondimensionalized by c_r

z = physical normal coordinate nondimensionalized by c_r

α = angle of attack

β = viscous ramp wedge angle

γ = specific heat ratio

Γ = jump in potential across wake

δ = boundary-layer thickness

δ^* = displacement thickness, $\int_0^\infty \left(1 - \frac{\rho U}{\rho_e U_e}\right) dN$

δ_ξ, δ_η, $\delta_{\zeta\zeta}$ = finite difference operators

$\Delta\xi, \Delta\eta, \Delta\zeta, \Delta t$ = finite difference numerical mesh step sizes

ϵ_1, ϵ_2 = $\begin{cases} 0 & \text{low frequency approximation} \\ 1 & \text{otherwise} \end{cases}$

ζ = nondimensional transformed normal coordinate

η = nondimensional transformed spanwise cordinate

θ = momentum defect thickness, $\int_0^\infty \frac{\rho U}{\rho_e U_e} \left(1 - \frac{U}{U_e}\right) dN$

$\left(\frac{\theta}{U_e} \frac{dU_e}{dS}\right)_{EQ}$ = see Eq. A-18

Λ_{LE} = leading edge sweep angle

Λ_s = local section sweep angle

λ = taper ratio

λ_c = see Eq. A-17

μ = viscosity coefficient

ξ = nondimensional transformed streamwise coordinate

ξ_o = offset of viscous ramp leading edge from sonic point

ξ_p = length of viscous ramp precursor

ξ_R = length of viscous ramp main body

ξ_s = sonic point location

ρ = density

ϕ = perturbation velocity potential function nondimensionalized by $c_r U_\infty$

Φ = physical velocity potential function, $c_r U_\infty (x + \phi)$

ω = circular oscillation frequency

Superscript

$+$ = upper surface

$-$ = lower surface

$\leftarrow$ = backward difference

$\sim$ = first intermediate solution (prediction)

$\approx$ = second intermediate solution (first correction)

$*$ = critical value

$\hat{}$	= symbolic representation
n	= previous time level
n + 1	= final solution at new time level (second correction)

Subscripts

e	= boundary-layer edge
I, J, K	= ξ, η, ζ grid indices
K_p	= ζ - plane lying above wing surface
K_m	= ζ - plane lying below wing surface
LE	= leading edge
min	= minimum
tip	= wing tip
t	= time derivative
US	= upstream
x,y,z ξ,η,ζ	= spatial derivative
2D	= two-dimensional
3D	= three-dimensional
∞	= freestream

I. INTRODUCTION

Solutions of steady inviscid transonic flowfields about wings of arbitrary planform are commonly obtained by numerical solution of the differential equation governing the velocity potential function. While this approach necessarily implies that any embedded shock waves are sufficiently weak that rotationality effects may be neglected, it has proven extremely useful for many applications[1-7]. In the case of unsteady flows, few methods capable of generating time accurate three-dimensional flowfields are currently available[8-12]. If the wing may be considered thin, the problem is rendered more tractable by applying the small disturbance assumption. This not only simplifies the governing equation, but also facilitates application of the surface boundary condition.

Time integration of the modified unsteady transonic small disturbance potential equation has proven to be particularly useful. It permits the treatment of nonlinear unsteady three-dimensional flow phenomena including irregular shock wave motion. In addition, the flowfield equation may be coupled directly with the structural equations of motion for an elastic wing which are simultaneously integrated in time in order to obtain a nonlinear aeroelastic solution[13].

Although unsteady inviscid flowfield solutions can provide a reasonable physical description for a wide variety of flow conditions, they will not be adequate when viscous effects are significant. This is typically true for flows about wings having advanced airfoil sections which involve complex flow structures characterized by the following phenomena: 1) shock-boundary-layer interaction altering the shock strength and location, 2) effective camber modification due to differences in the boundary-layer displacement on the upper and lower wing surfaces, and 3) displacement and camber effects of the near wake. A detailed description of these effects can be provided only through the use of additional equations governing the flow. Numerical solution of the more exact equations appropriate to three-dimensional viscous flows is burdensome in terms of computing resources. For the study of

aeroelastic behavior and nonlinear flutter, it is reasonable to perform a more simplified analysis. It is the intent here to account for the gross dominant effects of inviscid/viscous interaction for such applications without degrading the basic efficiency of the inviscid computation. Thus, no attempt will be made to resolve exact details of viscous regions, but rather the effects of viscosity upon the unsteady surface pressure distribution will be determined in order to provide appropriate aerodynamic forces for structural applications.

It is assumed that viscous effects are confined to thin regions immediately adjacent to the wing surface and along the trailing wake. These are then postulated to be in instantaneous equilibrium with the unsteady outer inviscid flow. A simple order of magnitude analysis indicates that this assumption is valid if the reduced frequency of the unsteady wing surface motion is small[14]. As a consequence, a steady form of the equations governing the viscous regions may be applied in a quasi-steady fashion. In addition, the viscous equations appropriate for two-dimensional flows will be applied stripwise along the span. For this calculation, however, the streamwise direction is taken as that either normal to the mean of the leading and trailing edge sweep angles for locally subsonic strips, or normal to the shock surface for strips where shock waves are present. Thus, the treatment of the viscous equations embodies the concept of simple sweep theory.

The use of two-dimensional boundary-layer equations greatly reduces the amount of computational effort involved in treating viscous regions. Even with an integral formulation, a three-dimensional viscous analysis requires solution of a system of partial differential equations, which can be costly. This is no small consideration for performing aeroelastic analysis which may require a large number of solutions to establish flutter boundaries.

Viscous regions are assumed to be governed by a set of boundary-layer equations appropriate for turbulent flows. For this purpose an integral form of "lag entrainment equations" are employed, which have been used with success for the prediction of turbulent shear layers[15-17]. Coupling with the outer inviscid flow is provided by the displacement thickness concept within the

framework of small disturbance theory. The impact of viscous effects upon the potential equation is manifested solely in a modification of the surface and wake boundary conditions. This procedure has proven adequate for a number of both steady and unsteady computations of flows about airfoils[18-20].

The most complex aspect of viscous transonic flows over airfoils is that of the shock-boundary-layer interaction. This effect is difficult to represent and resolve correctly for turbulent flows, and troublesome to couple in a numerically stable fashion with the outer inviscid solution. In the case of steady flows, procedures have been developed which achieve this coupling. Such methods commonly involve the use of underrelaxation in an iterative process such that a matching of the two solutions is obtained at convergence. Both the physical and numerical difficulties are considerably more involved in the unsteady case. Here the shock strength and location vary in time as the shock traverses the wing surface. In addition, time accuracy as well as stability is essential.

Much of this difficulty is removed by employing a simple computational artifice to model the displacement effect of the shock-boundary-layer interaction which is used in conjunction with the boundary-layer solution. This is accomplished by augmenting the wing surface geometry with a wedge-nosed ramp that is inserted near the base of the shock in the inviscid calculation. The ramp converts the normal shock to an oblique shock, thereby decreasing its strength, displaces it upstream from its inviscid location, and is free to traverse the wing surface in correspondence with the unsteady shock motion. The magnitude of the ramp angle is allowed to adjust instantaneously to the shock strength and is chosen such that an empirically defined post-shock pressure is recovered. Application of this ramp model has proven quite useful in both two- and three-dimensional steady computations[21] and more recently in two-dimensional unsteady solutions[14,22].

II. UNSTEADY POTENTIAL EQUATION

The equation governing the outer inviscid flow is the modified three-dimensional unsteady transonic small disturbance potential equation which includes higher order terms to ensure proper swept shock jump conditions, and may be written as

$$\frac{\partial}{\partial t}(A\phi_t + B\phi_x) = \frac{\partial}{\partial x}(E\phi_x + F\phi_x^2 + G\phi_y^2)$$

$$+ \frac{\partial}{\partial y}(\phi_y + H\phi_x\,\phi_y) + \frac{\partial}{\partial z}(\phi_z) \quad . \tag{1}$$

Here ϕ is the perturbation velocity potential function and

$$A = \varepsilon_1 M_\infty^2 k^2, \tag{2a}$$

$$B = 2 M_\infty^2 k, \tag{2b}$$

$$E = 1 - M_\infty^2, \tag{2c}$$

$$F = -1/2 (\gamma + 1) M_\infty^2, \tag{2d}$$

$$G = 1/2 (\gamma - 3) M_\infty^2, \tag{2e}$$

$$H = -(\gamma - 1) M_\infty^2, \tag{2f}$$

where k is the nondimensional time scaling.

The following shearing transformation is applied in order to map the swept tapered wing planform in the physical domain into a rectangle in the Cartesian computational domain:

$$\xi = \frac{x - x_{LE}(y)}{c(y)}, \quad \eta = y, \quad \zeta = z. \tag{3}$$

Outboard of the wing tip, a smooth transition to a constant chord section swept at the average of the leading and trailing edge sweep angles is applied. In addition, the coefficient G is split into two components

$$G = G_S + G_N, \tag{4a}$$

$$G_S = 1 - M_\infty^2, \tag{4b}$$

$$G_N = 1/2\ (\gamma - 1)\ M_\infty^2 - 1, \tag{4c}$$

such that the streamwise and normal contributions to the spatial differencing of the governing equation may be identified. This decomposition will be useful in the formulation of the numerical solution algorithm. Upon defining

$$a = \left(\frac{E}{c}\right) + 2\ G_S\ \xi_y\ \phi_\eta, \tag{5a}$$

$$b = \left(\frac{F}{c^2}\right) + G_S\ \xi_y^2, \tag{5b}$$

$$X = G_N\ (\xi_y\ \phi_\xi + \phi_\eta)^2 + H\xi_y\ \phi_\xi\ (\xi_y\ \phi_\xi + \phi_\eta) + c\ \xi_y\ (\xi_y\ \phi_\xi + \phi_\eta), \tag{5c}$$

$$Y = H\phi_\xi\ (\xi_y\ \phi_\xi + \phi_\eta) + c\xi_y\ \phi_\xi \tag{5d}$$

Eq. 1 becomes

$$cA\phi_{tt} + B\phi_{\xi t} = \frac{\partial}{\partial\xi}\ (a\ \phi_\xi + b\ \phi_\xi^2) + 2\ G_S\ \phi_\eta\ \phi_{\xi\eta} + \frac{\partial}{\partial\eta}\ (\ c\ \phi_\eta) + c\frac{\partial^2\phi}{\partial\zeta^2} + \frac{\partial X}{\partial\xi} + \frac{\partial Y}{\partial\eta}\ . \tag{6}$$

It is noted that

$$\frac{\partial}{\partial\xi}\ (a\ \phi_\xi + b\ \phi_\xi^2) + 2\ G_S\ \phi_\eta\ \phi_{\xi\eta} \tag{7}$$

represents the streamwise contribution to the governing equation with the remaining terms on the right-hand side of Eq. 6 comprising the normal portion.

A formal definition of the inviscid problem is completed by prescription of the boundary and initial conditions:

$$\text{far upstream} \quad \phi = 0, \tag{8a}$$

$$\text{far downstream} \quad \frac{1}{c}\phi_\xi + \epsilon_2 k\, \phi_t = 0, \tag{8b}$$

$$\text{wing root} \quad \xi_y\, \phi_\xi + \phi_\eta = 0, \tag{8c}$$

$$\text{far spanwise} \quad \phi_\eta = 0, \tag{8d}$$

$$\text{far above and below} \quad \phi_\zeta = 0. \tag{8e}$$

On the wing surface, the linearized unsteady boundary condition

$$\phi_\zeta^{\pm} = \frac{1}{c} f_\xi^{\pm} + \epsilon_1 k f_t^{\pm} \tag{9}$$

is applied on $\zeta = 0^{\pm}$ for $0 \le \xi \le 1$, $0 \le \eta \le \eta_{tip}$.

Along the trailing vortex sheet in the wake, the following contact conditions are invoked:

$$\left[\frac{1}{c}\phi_\xi + \epsilon_2 k\, \phi_t\right] = 0, \tag{10a}$$

$$[\phi_\zeta] = 0, \tag{10b}$$

on $\zeta = 0$ for $\xi > 1$, $0 \le \eta \le \eta_{tip}$, where brackets denote the jump in the enclosed quantity from above to below the vortex sheet.

Finally, the initial conditions

$$\phi\,(\xi,\eta,\zeta,0) = g\,(\xi,\eta,\zeta),\ \phi_t\,(\xi,\eta,\zeta,0) = h(\xi,\eta,\zeta) \tag{11}$$

are specified.

Once the solution to Eq. 6 is obtained, the local instantaneous pressure coefficient may be determined from the following expression

$$C_p = -2\left(\frac{1}{c}\phi_\xi + \epsilon_1 k\, \phi_t\right). \tag{12}$$

III. VISCOUS EQUATIONS

Solution of the equations governing viscous flow regions is predicated upon the quasi-study assumption. Therefore, it is necessary to consider only the steady form of the equations involved in order to extend the flowfield solution from time level t^n to time level $t^{n+1} = t^n + \Delta t$ during the unsteady solution process. In order to evaluate viscous parameters at the new time level, t^{n+1}, all inviscid quantities are obtained from the potential solution at time level t^n. The two-dimensional form of the viscous equations is employed stripwise along the span. However, the streamwise direction is taken as that normal to the local sweep angle, Λ_s. The value of Λ_s is equal to that of the incident shock surface for locally supersonic strips or the mean of the leading and trailing edge sweep angles for locally subsonic strips.

Viscous Ramp

The viscous ramp model, which is used to simulate the displacement effect of the shock-boundary-layer interaction, is based upon the observation in many steady experimental measurements that the post-shock pressure level for turbulent flow over an airfoil corresponds approximately to that of the oblique shock produced by flow over a compression ramp with a wedge angle equal to that of the detachment angle for the given upstream Mach number. Geometry of the model is depicted schematically in Figure 1. It consists of a short precursor over which the ramp slope varies linearly from zero to the given wedge angle followed by the main ramp body along which the slope varies quadratically. At the ramp leading edge the ramp height and slope are continuous, and at the downstream end and the slope and curvature vanish. The ramp is positioned with respect to the local instantaneous sonic point location and affinely scaled with the shock strength as determined by local conditions upstream of the shock. By offsetting the ramp leading edge a distance ξ_0 ahead of the sonic location, the ramp is able to more fully influence the numerical shock profile. The leading edge of the ramp is preceded by a precurser of length ξ_p which has been used in previous

unsteady calculations[14,20,22] to moderate passage of the sharp leading edge across computational mesh points, thereby precluding spurious numerical instabilities. The main body of the ramp has a length of ξ_R where the parameters ξ_p, ξ_o, and ξ_R may be selected for each specific application.

The wedge angle, β, is obtained directly from the steady two-dimensional form of Eq. 6. A complete derivation may be found in Ref. 20. In addition, the concepts of simple sweep theory are applied to obtain

$$\beta = \left(\frac{2}{F}\right)\left[\frac{-2\cos^2\Lambda_s\left(\frac{F}{c}\right)\phi_{\xi_{US}} - E}{3}\right]^{3/2} \tag{13}$$

where $\phi_{\xi_{US}}$ is evaluated just upstream of the shock. Given $\phi_{\xi_{US}}$ and the sonic point location, ξ_s, the ramp slope variation f_{R_ξ} is defined as follows:

$$f_{R_\xi}^{\pm} = 0 \text{ for } \xi < \xi_s - \xi_o - \xi_p, \tag{14a}$$

$$f_{R_\xi}^{\pm} = \pm\beta\left[1 + \frac{(\xi - \xi_s + \xi_o)}{\xi_R}\right] \text{ for} \tag{14b}$$

$$\xi_s - \xi_o - \xi_p \le \xi \le \xi_s - \xi_o,$$

$$f_{R_\xi}^{\pm} = \pm\beta\left[1 - \frac{(\xi - \xi_s + \xi_o)}{\xi_R}\right]^2 \text{ for} \tag{14c}$$

$$\xi_s - \xi_o \le \xi \le \xi_s - \xi_o + \xi_R$$

$$f_{R_\xi}^{\pm} = 0 \text{ for } \xi > \xi_s - \xi_o + \xi_R. \tag{14d}$$

Lag Entrainment Equations

The form of the integral boundary-layer equations which will be considered here is that of the lag entrainment equations due to Green[15]. They are predicated upon the boundary-layer assumption that the normal extent of viscous regions is small compared to the wing or wake thickness, which necessarily applies to flows at high Reynolds numbers. By integrating the governing partial differential equations in the normal direction and suitably modelling the requisite relationships among the dependent variables, a system of three first order ordinary differential equations is obtained. Two of the equations result directly from continuity and momentum. The third evolves from the Bradshaw, Ferriss, and Atwell[23] turbulent energy equation, but is formulated in terms of the entrainment concept originally proposed by Head[24]. This yields a streamwise rate equation governing the degree to which the outer inviscid flow merges with the turbulent shear layer.

The lag entrainment equations are beiefly summarized here, where the simple sweep concept has been employed for coupling with the inviscid solution. We first define

$$\text{displacement thickness } \delta^* = \int_0^\infty \left(1 - \frac{\rho U}{\rho_e U_e}\right) dN, \tag{15}$$

$$\text{momentum defect thickness } \theta = \int_0^\infty \frac{\rho U}{\rho_e U_e}\left(1 - \frac{U}{U_e}\right) dN, \tag{16}$$

$$\text{shape factor } \quad H_0 = \frac{\delta^*}{\theta}, \tag{17}$$

$$\text{shape parmeter } \overline{H} = \frac{1}{\theta} \int_0^\infty \frac{\rho}{\rho_e}\left(1 - \frac{U}{U_e}\right) dN, \tag{18}$$

$$\text{entrainment coefficient } \quad C_E = \frac{1}{\rho_e U_e} \frac{d}{dS} \int_0^\delta \rho U \, dN. \tag{19}$$

Here S and N are the streamwise and normal directions respectively within the boundary layer. The subscript e refers to the boundary-layer edge denoted by $N = \delta$. Within the confines of small disturbance theory the edge conditions

may be taken as those corresponding to the inviscid solution along the wing surface or wake centerline evaluated on $\zeta = 0^{\pm}$.

The primary dependent variables are taken as $(\frac{\theta}{c_s})$, $\overline{H}$, and C_E. Given their value at any streamwise station, ξ, their distributions may be predicted by the following system of first order ordinary differential equations:

$$\frac{d}{d\xi}\left(\frac{\theta}{c_s}\right) = \frac{C_f \cos \Lambda_s}{2} - [H_o + 2 - M_e^2 \cos^2 \Lambda_s] \left(\frac{\theta}{c_s}\right) \left(\frac{1}{c}\right) \phi_{\xi\xi}, \tag{20}$$

$$\frac{d\overline{H}}{d\xi} = \left(\frac{\theta}{c_s}\right)^{-1} \frac{d\overline{H}}{dH_1}\left\{C_E \cos \Lambda_s - H_1 \left[\frac{C_f \cos \Lambda_s}{2} - (H_o + 1) \left(\frac{\theta}{c_s}\right) \left(\frac{1}{c}\right) \phi_{\xi\xi}\right]\right\}, \tag{21}$$

$$\frac{dC_E}{d\xi} = \left(\frac{\theta}{c_s}\right)^{-1} F_A \left\{\left(\frac{2.8}{H_o + H_1}\right) \cos \Lambda_s [(C_\tau)_{EQ_o}^{1/2} - \lambda_c (C_\tau)^{1/2}] + \left(\frac{\theta}{U_e} \frac{dU_e}{dS}\right)_{EQ} \cos \Lambda_s \right.$$

$$\left. - [1 + 0.075 M_e^2 \cos^2 \Lambda_s \left(\frac{1 + 0.2 M_e^2 \cos^2 \Lambda_s}{1 + 0.1 M_e^2 \cos^2 \Lambda_s}\right)] \left(\frac{\theta}{c_s}\right) \left(\frac{1}{c}\right) \phi_{\xi\xi} \right\} \tag{22}$$

A definition of the parameters necessary to complete the description of these equations is given in Appendix A.

Using Eqs. 17 and A-12 it may be shown that

$$\left(\frac{\delta^*}{c_s}\right)_\xi = F_1 + F_2 \phi_{\xi\xi} \tag{23}$$

where

$$F_1 = \left\{\frac{H_o C_f}{2} + \left[1 + \left(\frac{\gamma - 1}{2}\right) r M_e^2\right] \left(C_E - \frac{H_1 C_f}{2}\right) \frac{d\overline{H}}{dH_1}\right\} \cos \Lambda_s \tag{24}$$

and

$$F_2 = \left\{\left[1 + \left(\frac{\gamma - 1}{2}\right) r M_e^2\right] (H_o + 1) H_1 \frac{d\overline{H}}{dH_1} + (\gamma - 1) r M_e^2 \left[1 + \left(\frac{\gamma - 1}{2}\right) r M_e^2\right] (\overline{H} + 1) \right.$$

$$\left. - H_o (H_o + 2 - Me^2)\right\} \left(\frac{\theta}{c_s}\right) \left(\frac{1}{c}\right). \tag{25}$$

This form was first deduced by East[17] et al. and displays the dominant explicit dependence of the displacement surface slope upon the pressure gradient $\phi_{\xi\xi}$.

Modified Boundary Conditions

The effect of the viscous flow regions is accounted for in the inviscid solution by modifying the surface boundary condition to incorporate viscous displacement. Thus, Eq. 9 is replaced by

$$\phi_\zeta^{\pm} = \frac{1}{c} f_\xi^{\pm} + \epsilon_1 k f_t^{\pm} + f_{R_\xi}^{\pm} \tag{26}$$

where the viscous ramp is used, and

$$\begin{aligned}\phi_\zeta^{\pm} &= \frac{1}{c} f_\xi^{\pm} + \epsilon_1 k f_t^{\pm} + \left(\frac{\delta^*}{c_s}\right)_\xi^{\pm} \\ &= \frac{1}{c} f_\xi^{\pm} + \epsilon_1 k f_t^{\pm} + (F_1 + F_2\, \phi_{\xi\xi})^{\pm}\end{aligned} \tag{27}$$

on $\zeta = 0^{\pm}$ for $0 \le \xi \le 1$, $0 \le \eta < \eta_{tip}$

when coupled with the lag entrainment equations. Downstream of the wing trailing edge the viscous wake generates an effective displacement afterbody. Due to its presence, a discontinuity in the slope of the potential is now permitted such that the wake condition Eq. 10b is replaced by

$$\begin{aligned}&[\phi_\zeta] = \left[\left(\frac{\delta^*}{c_s}\right)_\xi\right] = [F_1 + F_2\, \phi_{\xi\xi}] \\ &\text{on } \zeta = 0 \text{ for } \xi > 1,\ 0 \le \eta \le \eta_{tip}.\end{aligned} \tag{28}$$

IV. NUMERICAL METHOD

Inviscid Algorithm

The time accurate solution of the inviscid potential equation (Eq. 6) is obtained by the following first-order (in time) accurate approximate factorization alternating direction implicit (ADI) algorithm:

i) ξ - sweep:

$$B\overleftarrow{\delta}_\xi \left(\frac{\tilde{\phi} - \phi^n}{\Delta t}\right) = D_\xi \left[a^n \left(\frac{\tilde{\phi}_\xi + \phi_\xi^n}{2}\right) + b\, \phi_\xi^n\, \tilde{\phi}_\xi\right]$$
$$+ 2\, G_S\, (\delta_\eta \phi^n)\, D_\eta\, (\overleftarrow{\delta}_\xi \phi^n) + \delta_\eta\, (c\, \delta_\eta \phi^n) \qquad (29a)$$
$$+ c\, \delta_{\zeta\zeta} \phi^n + \delta_\xi X^n + \delta_\eta Y^n ,$$

ii) η - sweep:

$$B\, \overleftarrow{\delta}_\xi \left(\frac{\tilde{\tilde{\phi}} - \tilde{\phi}}{\Delta t}\right) = \frac{1}{2}\, \delta_\eta\, (c\, \delta_\eta\, \tilde{\tilde{\phi}} - c\, \delta_\eta\, \phi^n)$$
$$+ G_S\, (\delta_\eta \phi^n)\, D_\eta\, (\overleftarrow{\delta}_\xi\, \tilde{\tilde{\phi}} - \overleftarrow{\delta}_\xi \phi^n), \qquad (29b)$$

iii) ζ - sweep:

$$cA \left(\frac{\phi^{n+1} - 2\phi^n + \phi^{n-1}}{\Delta t^2}\right) + B\, \overleftarrow{\delta}_\xi \left(\frac{\phi^{n+1} - \tilde{\tilde{\phi}}}{\Delta t}\right)$$
$$= \frac{c}{2}\, \delta_{\zeta\zeta}\, (\phi^{n+1} - \phi^n). \qquad (29c)$$

Here, δ_ξ, δ_η, and $\delta_{\zeta\zeta}$ are second-order accurate central difference operators, $\overleftarrow{\delta}_\xi$ is a first-order accurate backward difference operator, and D_ξ and D_η are type-dependent mixed difference operators. Details of the numerical method are summarized in Ref. 10 and discussed in detail in Ref. 25.

Viscous Equations

The viscous ramp slope modification at time level n+1 ($f_{R_\xi}^{n+1}$) is evaluated based upon the potential distribution at time level n (ϕ^n). In order to locate the sonic point, ξ_s, the simple sweep relationship

$$C_{p_{2D}} = C_{p_{3D}} / \cos^2 \Lambda_s \tag{30}$$

is employed, where the steady form of $C_{p_{3D}}$ is taken as is consistent with the quasi-steady assumption. The sonic point is then defined such that

$$C_{p_{2D}} = C^*_{p_{2D}} \quad \text{at } \xi = \xi_s. \tag{31}$$

The critical pressure coefficient, $C^*_{p_{2D}}$, is that corresponding to the equivalent two-dimensional freestream Mach number

$$M_{\infty_{2D}} = M_{\infty_{3D}} \cos \Lambda_s. \tag{32}$$

The upstream location at which $\phi_{\xi_{US}}$ is evaluated corresponds to that grid point lying two mesh point upstream of ξ_s. Once ξ_s and $\phi_{\xi_{US}}$ are obtained, the entire ramp geometry is defined by Eqs. 13 and 14.

Solutions to the lag entrainment equations in the form given by Eqs. 20 to 22 are obtained by a simple second-order accurate Runge-Kutta integration scheme. Initial conditions are established upstream of shock waves for sections where the flow is locally supersonic or at the point of minimum pressure for sections where shock waves are absent. For this purpose incompressible flat plate results and a 1/7 power law velocity profile[28] are used to initialize θ, $\overline{H}$, and C_ξ. Integration is then carried out to the downstream boundary based upon the potential distribution at the previous time step.

Coupling Procedure

Far upstream of shock waves all viscous effects upon the inviscid solution are neglected. For locally supersonic stations the viscous ramp is employed ahead of the sonic location as a simple wing surface slope modification given by Eq. 26, but no coupling with the boundary-layer solution is involved. Downstream of the sonic location the remaining portion of the viscous ramp is ignored and the boundary-layer solution is implicitly coupled to the inviscid solution through use of Eqs. 27 and 28. In the case of locally subsonic stations no viscous ramp is employed and the implicit coupling procedure is initiated at the point of minimum pressure.

The wing plane ($\zeta = 0$) is centered between planes of computational mesh points, such that the surface boundary condition is manifested in the calculation of $\phi_{\zeta\zeta}$ in the mesh planes just above and below $\zeta = 0$. This is accomplished by employing the relationship

$$(\phi_{\zeta\zeta})_{IJK_p} = (\frac{1}{\Delta\zeta})^2 [(\phi_{IJK_p+1} - \phi_{IJK_p}) - \Delta\zeta\ (\phi_\zeta^+)_{IJ}] \tag{33}$$

where the index K_p refers to the mesh plane just above the wing surface and a constant mesh size is considered here for illustrative purposes. The surface boundary condition is now employed as

$$(\phi_\zeta^+)_{IJ} = \frac{1}{c_J} (f_\xi^+)_{IJ} + \epsilon_1 k (f_t^+)_{IJ} + (F_1^+ + F_2^+ \phi_{\xi\xi}^+)_{IJ}, \tag{34}$$

and $(\phi_{\xi\xi}^+)_{IJ}$ is written in terms of the potential at points lying above the surface; i.e.

$$(\phi_{\xi\xi}^+)_{IJ} = (\frac{1}{\Delta\zeta}) [\zeta_{K_p+1} (\phi_{\xi\xi})_{IJK_p} - \zeta_{K_p} (\phi_{\xi\xi})_{IJK_p+1}]. \tag{35}$$

Equations 34 and 35 are then used in conjunction with Eq. 33 to obtain

$$(\phi_{\zeta\zeta})^{n+1}_{IJK_p} = (\frac{1}{\Delta\zeta})^2 \Big\{ (\phi^{n+1}_{IJK_p+1} - \phi^{n+1}_{IJK_p})$$

$$- \Delta\zeta \, [\frac{1}{c_J} (f_\xi^+)^{n+1}_{IJ} + \varepsilon_1 k (f_t^+)^{n+1}_{IJ} + (F_1^+)^n_{IJ}]$$

$$- (\frac{1}{\Delta\xi})^2 (F_2^+)^n_{IJ} \, [\zeta_{K_p+1} (\phi^n_{I+1\,JK_p} - 2\,\phi^{n+1}_{IJK_p} + \phi^{n+1}_{I-1\,JK_p})$$

$$- \zeta_{K_p} (\phi^n_{I+1\,JK_p+1} - 2\,\phi^{n+1}_{IJK_p+1} + \phi^{n+1}_{I-1\,J\,K_p+1})] \Big\} . \qquad (36)$$

This expression forms an implicit relationship as part of the tri-diagonal system in the ζ - sweep of the inviscid algorithm. An expression similar to Eq. 36 may be derived for $(\phi_{\zeta\zeta})^{n+1}_{IJK_m}$. It is noted that at the grid location I, J valu of ϕ at the upstream column $(\phi^{n+1}_{I-1\,J})$ are known at the advanced time level but those at the downstream column $(\phi^n_{I+1\,J})$ must be taken at the previous time level for the algorithm to remain intact. The coupling procedure is considered to be significant in suppressing numerical instabilities which would otherwise occur, particularly in regions where $(\frac{\delta^*}{c_s})_\xi$ is large such at the trailing edge.

Along the trailing wake the following relationship is employed

$$(\phi_{\zeta\zeta})_{IJK_p} = (\frac{1}{\Delta\zeta})^2 \, (\phi_{IJK_p+1} - 2\phi_{IJK_p} + \hat{\phi}_{IJK_m}) \qquad (37)$$

where $\hat{\phi}_{IJK_m}$ is a symbolic representation of the value of ϕ_{IJK_m} which incorporates the jump in ϕ and ϕ_ζ across $\zeta = 0$ and K_m refers to the mesh plane just below $\zeta = 0$. By analytic continuation (i.e., Taylor Series) $\hat{\phi}_{IJK_m}$ may be expressed in terms of values along $\zeta = 0^+$, i.e.

$$\hat{\phi}_{IJK_m} = \phi^+_{IJ} - (\frac{\Delta\zeta}{2}) \, (\phi^+_\zeta)_{IJ} . \qquad (38)$$

Similarly, the value of ϕ_{IJK_m} may be written in terms of values along $\zeta = 0^-$ as

$$\phi_{IJK_m} = \phi^-_{IJ} - \left(\frac{\Delta\zeta}{2}\right)(\phi^-_\zeta)_{IJ} \cdot \tag{39}$$

Combining Eqs. 38 and 39 results in

$$\hat{\phi}_{IJK_m} = \phi_{IJK_m} + (\phi^+_{IJ} - \phi^-_{IJ}) - \left(\frac{\Delta\zeta}{2}\right)[(\phi^+_\zeta)_{IJ} - (\phi^-_\zeta)_{IJ}]. \tag{40}$$

For convenience we now define

$$(\phi^+_{IJ} - \phi^-_{IJ}) = \Gamma_{IJ} \tag{41}$$

and express the jump in the normal slope of the potential across the trailing wake in accordance with Eq. 28 as

$$[(\phi^+_\zeta)_{IJ} - (\phi^-_\zeta)_{IJ}] = [(F^+_1)_{IJ} + (F^+_2)_{IJ}(\phi^+_{\xi\xi})_{IJ}] - [(F^-_1)_{IJ} + (F^-_2)_{IJ}(\phi^-_{\xi\xi})_{IJ}]. \tag{42}$$

From Eq. 41 it follows that

$$(\phi^-_{\xi\xi})_{IJ} = (\phi^+_{\xi\xi})_{IJ} - (\Gamma_{\xi\xi})_{IJ}. \tag{43}$$

Using Eq. 35 and substituting Eqs. 41 to 43 into Eq. 40, it may be shown that

$$\hat{\phi}_{IJK_m} = \phi_{IJK_m} + \Gamma_{IJ} - \left(\frac{\Delta\zeta}{2}\right)[(F^+_1)_{IJ} - (F^-_1)_{IJ}] - \frac{1}{2}[(F^+_2)_{IJ} - (F^-_2)_{IJ}][\zeta_{K_p+1}(\phi_{\xi\xi})_{IJK_p} - \zeta_{K_p}(\phi_{\xi\xi})_{IJK_p+1}] - \left(\frac{\Delta\zeta}{2}\right)(F^-_2)_{IJ}(\Gamma_{\xi\xi})_{IJ}. \tag{44}$$

Finally, Eq. 44 is substituted into Eq. 37 to obtain

$$(\phi_{\zeta\zeta})^{n+1}_{IJK_p} = (\frac{1}{\Delta\zeta})^2 (\phi^{n+1}_{IJK_p+1} - 2\phi^{n+1}_{IJK_p} + \phi^{n+1}_{IJK_m} + \Gamma^{n+1}_{IJ})$$

$$- (\frac{1}{2\Delta\zeta}) [(F_1^+)^n_{IJ} - (F_1^-)^n_{IJ}]$$

$$- (\frac{1}{2}) (\frac{1}{\Delta\zeta})^2 (\frac{1}{\Delta\xi})^2 [(F_2^+)^n_{IJ} - (F_2^-)^n_{IJ}] [\zeta_{K_p+1} (\phi^n_{I+1JK_p} - 2\phi^{n+1}_{IJK_p} + \phi^{n+1}_{I-1\ JK_p})$$

$$- \zeta_{K_p} (\phi^n_{I+1\ JK_p+1} - 2\phi^{n+1}_{IJK_p+1} + \phi^{n+1}_{I-i\ JK_p+1})]$$

$$- (\frac{1}{2\Delta\zeta}) (\frac{1}{\Delta\xi})^2 (F_2^-)^n_{IJ} (\Gamma^n_{I+1J} - 2\Gamma^{n+1}_{IJ} + \Gamma^{n+1}_{I-1J}). \qquad (45)$$

An expession similar to Eq. 45 may be derived for $(\phi_{\zeta\zeta})^{n+1}_{IJK_m}$.

V. RESULTS

A computer program, XTRAN3S, based upon the inviscid numerical algorithm described above is available for calculating the steady and unsteady aerodynamic loads and aeroelastic response of thin clean wings in transonic flow. This code is fully described in Ref. 25 to 28. All of the results presented here were generated using XTRAN3S. The basic code has been modified to account for viscous effects by incorporating the previously described method. Appendix B describes alterations in user input specifications for the modified version of XTRAN3S.

For each of the cases considered, calculations were performed which generated an inviscid solution, a solution using the viscous ramp alone, and a full viscous solution employing the viscous ramp in conjunction with the boundary-layer equations.

All computations were performed on a nonuniform 60 x 20 x 40 (ξ, η, ζ) Cartesian computational mesh with the wing surface defined by 39 x 12 points in the ξ - η plane. The computational domain was defined by

$$-15.375 \leq \xi \leq 26.575$$

$$0 \leq \eta \leq 5.3$$

$$-13.0375 \leq \zeta \leq 13.0375$$

and minimum grid spacing taken as

$$\Delta\xi_{min} = 0.01$$

$$\Delta\eta_{min} = 0.10$$

$$\Delta\zeta_{min} = 0.025$$

which occur at the wing leading edge, at the wing tip, and adjacent to the wing surface respectively. XTRAN3S default values were employed for the ξ- and ζ-mesh distributions. The η-mesh and surface geometry description for each case considered may be found in Appendix C. For all calculations the time scaling, k, was selected as 0.2 and a time step of $\Delta t = 0.0034906585$ was employed. This corresponds to a distance of one root chord of travel in 57.3 time steps at the freestream velocity. For a reduced frequency of $k_c = 0.2$, the choice of Δt results in five time steps per degree of circular frequency change along the pitching cycle of a forced oscillation. Nominal values of the viscous ramp parameters were selected as follows:

$$\xi_o = 0.02,$$
$$\xi_p = 0.02,$$
$$\xi_R = 0.10.$$

These choices have proven adequate for a number of both steady and unsteady two-dimensional solutions[14,20]. Results were generated on the CRAY-1S computing system and required approximately 0.5 seconds of CPU time per time step of calculation for both inviscid and wedge alone solutions, and 0.6 seconds per time step for full viscous computations.

All converged steady state solutions were run for 900 time steps at the indicated values of k and Δt. These choices were found to be conservative with respect to both stability and convergence. The low frequency approximation (i.e., $\varepsilon_2 = 0$) was made in the wake jump condition Eq. 10a and downstream boundary condition Eq. 8b to prevent anomalous behavior which was otherwise observed to occur for swept tapered planforms. In general, the following procedure was employed in generating steady-state results:

i) a converged inviscid solution was obtained using an undisturbed condition as an initial state (i.e., $\phi = \phi_t = 0$);

ii) a converged wedge alone solution was obtained using the inviscid solution as the intiial state, updating the wedge computation at each time step;

iii a converged full viscous solution was obtained using the wedge alone solution as the initial state, updating the boundary-layer computation at each time step.

In order to establish validity of the assumptions underlying the computational method, comparison is made with experimental data for the steady flow about a high aspect ratio wing having an advanced airfoil section. The configuration to be considered is depicted schematically in Fig. 2 and corresponds to the Lockheed-Georgia "Wing A"[29,30] which was developed as part of a comprehensive program to acquire steady transonic experimental data specifically for evaluation of three-dimensional computational methods. The wing has an aspect ratio of 8.0, a taper ratio of 0.4, and leading edge sweep angle of 27^{0}. A nonuniform 12% thick airfoil section having appreciable aft camber is employed, with approximately 5^{0} of nose-down twist occurring between the root and tip sections. The section and planform geometry are regarded as representative of modern transport aircraft.

Freestream conditions were established for the flow in air at $M_{\infty} = 0.819$, $\alpha = 1.96^{0}$, and $Re_{\infty} = 8.08 \times 10^{6}$. These values duplicate the test conditions of Hinson and Burdges[29,30] as well as the numerical results of Streett[31]. Steady-state solutions were generated by the time integration procedure previously summarized. In the case of the full viscous computation it was not possible to obtain an entirely converged steady solution due to boundary-layer separation at the trailing edge of the upper surface and in the aft cove region of the lower surface. A reasonable result was arrived at by the following procedure. Using the converged wedge alone solution as an initial profile, a converged viscous solution was generated at a Reynolds number of 8.08×10^{7}. This value is 10 times that of the test condition and was sufficiently high to preclude boundary-layer separation. The computation was then restarted with the converged viscous result as the initial profile and run for 80 time steps at the test Reynolds number. In both calcuations the boundary-layer computation was updated each time step. The final solution is probably resolved to plotting accuracy in the pressure distribution. Any further calculation rapidly produced separation.

Results of the calculations are shown in Fig. 3 in terms of the wing surface pressure distributions where the data of Hinson and Burdges has been provided for comparison. The spanwise mesh distribution was selected to coincide with experimental data measuring stations. Comparison of the full viscous result with the inviscid solution indicates the improvement due to the boundary-layer calculation. It is noted that the shock is weakened and displaced forward by the inclusion of viscous effects. Aft decambering due to boundary-layer displacement is quite noticable, particularly on the aft lower surface. The wedge alone solution is seen to produce some anomalous behavior on the rearward portion of the upper surface. This is probably due to the post shock re-expansion and the high aft camber. The only spurious result from the full viscous solution is noted at $\eta/\eta_{tip} = 0.70$ immediately downstream of the shock, and may be caused by the merging of the wedge and boundary-layer slope modifications. In Ref. 31, the results of calculations from a pilot version of XTRAN3S were presented for the same case. In those calculations, the spike downstream of the shock shown in Fig. 3d was not observed.

In Figure 4 the full viscous result at $\eta/\eta_{tip} = 0.70$ is compared with another computational solution. The numerical results of Streett[32] consist of a full potential inviscid outer flow solution and a fully three-dimensional integral boundary-layer and wake solution coupled via the displacement thickness. While the flow conditions for Streett's solution are the same as noted previously, the configuration consists of a half-body fuselage model with a mid-mounted wing and corresponds to another of the test cases of Hinson and Burdges. Streett's results compared extremely well with experiment, thus, the data for the wing-body combination has been omitted. Due to the presence of the body, the shock lies somewhat ahead of its location for the wing alone. The lower surface pressure distribution is virtually the same in both cases.

Upper surface distributions of the displacement and momentum defect thickness at midspan appear in Fig. 5. Influence of the shock can be seen near $\xi = 0.4$. Downstream of the trailing edge, θ and δ^* tend to constant values which is consistent for wakes without pressure gradient.

In the case of fully three-dimensional unsteady transonic flows over wings, little experimental data suitable for validation purposes is available. Because of this, a representative sample calculation was selected in order to

illustrate results of the numerical method. For this example a section geometry corresponding to the MBB-A3[33] airfoil was chosen. The section, shown in Fig. 6, has a blunt leading edge, a thickness ratio of 8.9%, moderate aft camber, and has been selected as an AGARD standard for evaluating transonic aeroelastic analysis methods. A wing planform identical to the Lockheed-Georgia "Wing A" was employed (AR = 8.0, λ = 0.4) except that the leading edge sweep angle was set to 30°. The MBB-A3 section was chosen to avoid the problems with boundary-layer separation evidenced in the Lockheed Wing A calculation. Even though the airfoil is thinner, it still may be viewed as representative of a typical modern transport aircraft configuration.

Steady-state solutions were generated for freestream conditions corresponding to $M_{\infty} = 0.85$, $\alpha = 1.0^{\circ}$, and $Re_{\infty} = 10^7$. Results of the pressure distributions at half of the spanwise mesh stations are compared in Fig. 7. Viscous effects near shocks and on the aft lower surface are apparent. Corresponding chordwise distributions of the displacement and momentum defect thickness near the midspan station appear in Fig. 8.

Using the steady-state solutions as initial conditions, unsteady calculations were performed by specifying a forced rotation about the wing leading edge root such that $\alpha = 1^{\circ} + 1^{\circ} \sin t$. The reduced frequency, k_c, was chosen to be 0.2. Integration in time was allowed to proceed for two cycles of rotation. Figures 9 and 10 indicate the instantaneous surface pressure distributions for the inviscid, wedge alone, and fully viscous cases. The value of time here is referenced to the beginning of the second cycle and given in radians. At the maximum angle of attack, $\alpha = 2^{\circ}$, (Fig. 9) a large difference between the solutions, particularly near shocks is evident. While the difference between the solutions is less substantial at the minimum angle of attack, $\alpha = 0^{\circ}$ (Fig. 10), aft decambering due to viscous displacement is still appreciable. Corresponding values of the displacement and momentum defect thickness are given in Figures 11 and 12. It is noted that the large differences in δ^* and θ at the extremes of the oscillation cycle are brought about by the alternate formation and disappearance of the shock. In Fig. 13 the total wing unsteady lift and moment coefficient time histories are presented along with the angle of attack variation. Although there is little phase difference between the inviscid and viscous solution for this particular case, the difference in both mean value and magnitude of oscillation is significant.

VI. DISCUSSION AND CONCLUSIONS

A method has been presented for computing the unsteady three-dimensional transonic flowfield about thin wings of arbitrary planform and section geometry including the effects of inviscid/viscous interaction. Dominant effects of the shock-boundary-layer interaction were accounted for by a simple compuational artifice, while viscous regions adjacent to the wing surface and along the trailing wake were described by a set of integral equations appropriate for two-dimensional turbulent flows. Although this analysis was necessarily simplified, comparison with steady three-dimensional experimental data and a solution of more exact equations for a typical transport configuration indicates that it will be adequate for many practical applications. In addition, an example calculation of a wing oscillating in rotation indicated appreciable variation in unsteady aerodynamic force coefficients when viscous effects are accounted for. This behavior is typical of wings having advanced airfoil sections and may be a significant consideration when performing aeroelastic analysis.

Several comments regarding the operation and possible improvement of the modified version of XTRAN3S are appropriate here. No provision has been made in the present work for the existence of a laminar boundary layer. The reason for this is that the lag entrainment equations do not perform well at low Reynolds numbers. Ideally, a simple attachment line model or stagnation point solution followed by a laminar calculation and suitable transition criteria could easily be incorporated in order to establish initial conditions for the lag entrainment equations without altering the basic computational method. For the results considered here, the Reynolds numbers were sufficiently large such that for practical purposes the entire boundary layer could be considered turbulent and the upstream displacement effect could be ignored. This may not be possible in all cases. Wake curvature effects have been neglected entirely in the present work. These may be accounted for by a simple alteration of the basic wake jump condition, Eq. 10a[32]. It is indicated by the results of Streett[32] that wake curvature may have a significant impact upon the lower surface pressure distribution for wings having advanced airfoil sections.

The Lockheed-Georgia "Wing A" proved to be a severe test of the computational method. Separation was indicated for the experimental configuration due to the combination of thickness, camber, and flow conditions. This evidences a need for treating cases of practical interest where boundary-layer separation occurs and requires a reformulation of the boundary-layer solution method in the "inverse" mode. It should also be noted that the version of XTRAN3S employed for the calculations was designed to operate efficiently on the CRAY-1S computing system. The boundary-layer calculation method was implemented as a simple modification of the basic code, but does not take advantage of the vectorization capabilities of the CRAY-1S. This slows the viscous calculation somewhat, but it could easily be made more efficient.

It is not recommended that the wedge alone be used on wings having advanced airfoil sections. As was noted for the cases presented here, use of the wedge alone tended to produce spurious post shock re-expansions. This effect may be reduced by varying the wedge parameters (ξ_0, ξ_p, ξ_R) but that was not done here. For wings having more conventional sections it is expected that the wedge alone will be quite useful.

The method of time integration of fluid dynamic equations of motion offers a unique capabilty for performing aeroelastic analysis. Unsteady structural equations of motion governing the deformation of an elastic wing may be coupled with these directly and simultaneously integrated in time to determine the aeroelastic response of the combined system. This technique has already been applied for a purely inviscid flowfield,[13] and may easily be extended to include viscous effects by the described method. Addition of the integral equations for viscous calculations increases computation time (CPU) by about 20%, thus maintaining the basic efficiency of the inviscid algorithm. This consideration provided much of the motivation for employing a simplified viscous analysis, and appears to be justified for the purpose of structural applications.

APPENDIX A

Conditions at the edge of the boundary layer may be obtained from the inviscid solution along the wing surface or wake centerline evaluated on $\zeta = 0^{\pm}$. In particular, using the small disturbance assumption and simple sweep theory, we may write

$$M_e = \left\{ 1 + \left[1 + \frac{(\gamma - 1)}{2} M_\infty^2 \right] \left(\frac{1}{c}\right) \phi_\xi \right\} M_\infty \cos \Lambda_s, \tag{A-1}$$

$$\frac{\rho_e}{\rho_\infty} = 1 - \left(\frac{1}{c}\right) M_\infty^2 \phi_\xi, \tag{A-2}$$

$$\frac{T_e}{T_\infty} = 1 - (\gamma - 1) M_\infty^2 \left(\frac{1}{c}\right) \phi_\xi. \tag{A-3}$$

The viscosity ratio is obtained from the Sutherland viscosity law in the form

$$\frac{\mu_e}{\mu_\infty} = \left(\frac{T_e}{T_\infty}\right)^{3/2} \left[\frac{1 + \frac{S_0}{T_\infty}}{\frac{T_e}{T_\infty} + \frac{S_0}{T_\infty}} \right] \tag{A-4}$$

where S_0 is a constant for the specific gas under consideration ($S_0 = 110^0$K. for air). The adiabatic recovery factor, r, is chosen as a function of the turbulent Prandtl number

$$r = (Pr_t)^{1/3}. \tag{A-5}$$

The following parameters then completely define the lag entrainment equations

$$F_c = \left[1 + \left(\frac{\gamma - 1}{2}\right) r M_e^2 \right]^{1/2}, \tag{A-6}$$

$$F_r = 1 + 0.056 M_e^2, \tag{A-7}$$

$$Re_\theta = \frac{\rho_e U_e \theta}{\mu_e} \tag{A-8}$$

$$= \left(\frac{\rho_e}{\rho_\infty}\right)\left[1 + \left(\frac{1}{c}\right)\phi_\xi\right]\cos\Lambda_s\left(\frac{\theta}{c_s}\right)\left(\frac{\rho_\infty U_\infty c_r}{\mu_\infty}\right)\left(\frac{\mu_e}{\mu_\infty}\right)^{-1},$$

$$C_{fo} = \begin{cases} \left(\frac{1}{F_c}\right)\left[\frac{0.01013}{\log_{10}(F_r\, Re_\theta) - 1.02} - 0.00075\right] \text{ for wall boundary layers} \\ 0 \text{ for wake shear layers,} \end{cases} \quad \text{(A-9)}$$

$$\frac{H}{Ho} = \bar{H}\left\{1 - 6.55\left[\frac{C_{fo}}{2}(1 + 0.04\, M_e^2)\right]^{1/2}\right\}, \quad \text{(A-10)}$$

$$C_f = \begin{cases} \left[\frac{0.9}{\left(\frac{H}{Ho} - 0.4\right)} - 0.5\right] C_{fo} \text{ for wall boundary layers} \\ 0 \text{ for wake shear layers,} \end{cases} \quad \text{(A-11)}$$

$$H_o = (\bar{H} + 1)\left[1 + \left(\frac{\gamma-1}{2}\right) r\, M_e^2\right] - 1, \quad \text{(A-12)}$$

$$\frac{d\bar{H}}{dH_1} = -\left[\frac{(\bar{H} - 1)^2}{1.72 + 0.02\,(\bar{H} - 1)^3}\right], \quad \text{(A-13)}$$

$$H_1 = 3.15 + \left(\frac{1.72}{\bar{H} - 1}\right) - 0.01\,(\bar{H} - 1)^2, \quad \text{(A-14)}$$

$$F_A = \frac{0.02 C_E + C_E^2 + \left(\frac{0.8\, C_{fo}}{3}\right)}{0.01 + C_E}, \quad \text{(A-15)}$$

$$C_\tau = (1 + 0.1\, M_e^2)(0.024\, C_E + 1.2\, C_E^2 + 0.32\, C_{fo}), \quad \text{(A-16)}$$

$$\lambda_c = \begin{cases} 1 \text{ for wall boundary layers} \\ 1/2 \text{ for wake shear layers,} \end{cases} \quad \text{(A-17)}$$

$$\left(\frac{\theta}{U_e}\frac{dU_e}{dS}\right)_{EQ_o} = \left(\frac{1.25}{H_o}\right)\left[\frac{C_f}{2} - \frac{\left(\frac{\bar{H} - 1}{6.432\,\bar{H}}\right)^2}{1 + 0.04\, M_e^2}\right], \quad \text{(A-18)}$$

$$(C_E)_{EQ_o} = H_1 \left[\frac{C_f}{2} - (H_o + 1) \left(\frac{\theta}{U_e} \frac{dU_e}{dS}\right)_{EQ_o}\right], \tag{A-19}$$

$$(C_\tau)_{EQ_o} = (1 + 0.1\ M_e^2)\ [0.024\ (C_E)_{EQ_o} + 1.2\ (C_E)^2_{EQ_o} + 0.32\ C_{fo}], \tag{A-20}$$

$$\overline{C} = \frac{(C_\tau)_{EQ_o}}{(1 + 0.1\ Me^2)\ \lambda_c^2} - 0.32\ C_{fo}, \tag{A-21}$$

$$(C_E)_{EQ} = \left(\frac{\overline{C}}{1.2 + 0.0001}\right)^{1/2} - 0.01, \tag{A-22}$$

$$\left(\frac{\theta}{U_e} \frac{dU_e}{dS}\right)_{EQ} = \left[\frac{1}{H_1\ (H_o + 1)}\right] \left[\frac{H_1\ C_f}{2} - (C_E)_{EQ}\right]. \tag{A-23}$$

APPENDIX B

MODIFICATION OF XTRAN3S INPUT DATA REQUIREMENTS FOR VISCOUS CALCULATIONS

The input data required by XTRAN3S is in the form of a card deck or a card image file. All data is free field. Section A describes the input data deck structure while Section B spells out the required input cards for implementation of the viscous option and the associated formats and groundrules. This Appendix may be considered as a revision of Section V of Ref. 26, and should be used in conjunction with that Section.

A. Input Data Deck Structure

The input data deck for XTRAN3S has four levels of organization.

1. Program Deck - This includes all inputs (other than control cards which are discussed in Section VIII of Ref. 26) for one problem. The deck "boundaries" are

   first record - BEGIN PROBLEM DEFINITION

   last record - END OF PROBLEM

2. Data Section - A program deck is divided into data sections. Specifically, the deck is divided into the following ten data sections:

   1) Problem Definition Section
   2) Computational Control Section
   3) Computational Grid Section
   4) Geometry Section
   5) Boundary Condition Section
   6) Structural Modal Section
   7) Structural Matrix Section
   8) Checkpoint/Restart Section

9) Post-processing Section
10) Viscous Calculation Section

As noted previously, the first section must be the Problem Definition Section. The order of the remaining sections is immaterial. The first record in each section must be of the form "BEGIN etc." No section terminator is required.

3. Data Record - Sections are in turn divided into data records or statements. As noted above, the first record is of the form "BEGIN etc." In most cases the order of the remaining records in the section is immaterial. All exceptions to this rule are specifically noted. Record boundaries are governed by the following rules.

   - o If the last non-blank character on the card is a "+" then the record continues onto the next card.
   - o Maximum record length is 250 items.
   - o Record terminators are / or card boundaries.
   - o The space between / and the card boundary is "ignored" and hence is available for comments. If a record is only comment it must begin with */.

4. Data Item - Records are in turn composed of data items. This is the finest level of subdivision for the program deck. The delimiters or "boundaries" of items are of two types.

   - o colon : this is used at most once per record and then only after keywords.
   - o commas, blank spaces and record terminators.

B. Record Formats

The following ground rules concerning notation apply throughout this section.

a) [[ ]]-- Data items enclosed by double brackets have optional input formats. One or more of the indicated options must be selected.

b) [ ]-- Data items enclosed by brackets have optional input formats. Only one of the indicated options must be selected.

c) ( )-- Data items enclosed by parentheses have default values. If the default is acceptable for definition of the problem data, the particular item or items need not be input. All default values are defined in the descriptions of the input data.

d) ITEM -- An item typed in all upper case letters is called a key-word. At least the underlined portion of a key-word must be input. This is always the first four characters including trailing blanks.

e) Item -- An item with only the leading character typed in upper case denotes that it must either be selected from a list of system key-words or that it is identical to an item previously defined by the user.

f) item -- An item typed in all lower case letters is defined strictly by the user.

The formats for data sections 1 through 9 are given in Ref. 26. The additional data required for viscous calculations is given in Section 10, which follows.

10. Viscous Calculation Section

The purpose of this section is to specify the Viscous Calculation option if the user so desires. If this option is not desired, then this section should be omitted.

1) BEGIN VISCOUS FLOW PARAMETERS

This data record is used to indicate that processing of data associated with the Viscous Calculation is to follow. The following card statements (2-5) are optional and need only be input if values other than the defaults are to be specified. Data records 2-4 define data associated with the viscous wedge (all values are nondimensional by local section chord).

2) (SHOCK OFFSET DISTANCE: xoffst)

Input of the shock offset distance.
The default is SHOCK OFFSET DISTANCE: .02.

3) (PRECURSOR LENGTH: xprec)

Input of the precursor length.
The default is PRECURSOR LENGTH: .02.

4) (RAMP LENGTH: xramp)

Input of the ramp length.
The default is RAMP LENGTH: 0.10.

5) (CALCULATION INTERVAL: iblcal)

Input of the viscous flow calculation update interval for both wedge and boundary-layer computations.
The default is CALCULATION INTERVAL: 1

6) BOUNDARY-LAYER SOLUTION

This data record is required if the boundary-layer calculation is to be executed and it also is the first data record associated with the boundary-layer calculation. The following card statements (7-11) are optional and need only be input if values other than the default values are to be input.

7) (PRINT INTERVAL: iblprt)

Input of the boundary-layer print interval.
The default is PRINT INTERVAL: 50.

8) (REYNOLDS NUMBER: reyinf)

Input of the free stream Reynolds number based on root chord.
The default is REYNOLDS NUMBER: 1.0E7

9) (TEMPERATURE: tinf)

Input of the free stream temperature (degrees Kelvin).
The default is TEMPERATURE: 300.0

10) (SUTHERLAND LAW CONSTANT: s0)

Input of the Sutherland Law Constant (degrees Kelvin).
The default (defined for air) is SUTHERLAND LAW CONSTANT: 110.0.

11) (PRANDTL NUMBER: prt)

Input of the turbulent Prandtl number.
The default is PRANDTL NUMBER: 0.9

APPENDIX C

The η-mesh distribution and wing surface slope definition for the two geometries considered are given here. In each case the wing surface is represented as an analytic function having the following form:

$$a_0\xi^0 + a_{1/2}\xi^{1/2} + a_1\xi^1 + a_2\xi^2 + a_3\xi^3 + a_4\xi^4 + a_5\xi^5.$$

1. Lockheed Georgia "Wing A"

   a. η-mesh

Index	η
1	-0.21
2	0.00
3	0.21
4	0.42
5	0.63
6	0.83
7	1.11
8	1.39
9	1.94
10	2.25
11	2.50
12	2.65
13	2.75
14	2.80
15	2.90
16	3.05
17	3.30
18	3.80
19	4.30
20	5.30

b. surface geometry

	Root		Tip	
	Upper Surface	Lower Surface	Upper Surface	Lower Surface
a_0	0.023996815	0.023517482	-0.017931003	-0.017921293
$a_{1/2}$	0.210881410	-0.148954440	0.175083370	-0.192270830
a_1	-0.348816530	-0.010928663	0.019118126	0.371830370
a_2	0.418018550	-0.106489380	-0.494377680	-0.938122680
a_3	-0.637010050	0.391707720	1.12296990	1.757023200
a_4	0.395787680	0.150884270	-1.211785000	-0.989445110
a_5	-0.085424090	-0.324138620	0.426635820	0.024627938

2. MBB-A3 Wing

a. η-mesh

Index	η
1	-0.25
2	0.00
3	0.25
4	0.50
5	0.75
6	1.00
7	1.30
8	1.70
9	2.00
10	2.25
11	2.50
12	2.65
13	2.75
14	2.80
15	2.90
16	3.05
17	3.30
18	3.80
19	4.30
20	5.30

b. Surface Geometry

	Root		Tip	
	Upper Surface	Lower Surface	Upper Surface	Lower Surface
a_0	0.0	0.0	0.0	0.0
$a_{1/2}$	0.1064264	-0.1064262	0.1064264	-0.1064262
a_1	0.0051279	0.2190702	0.0051279	0.2190702
a_2	-0.1236988	-0.6049436	-0.1236988	-0.6049436
a_3	-0.0149070	0.9704346	0.0149070	0.9704346
a_4	0.0270518	-0.4781350	0.0270518	-0.4781350
a_5	0.0	0.0	0.0	0.0

REFERENCES

1. Ballhaus, W. F. and Bailey, F. R., "Numerical Calculation of Transonic Flow About Swept Wings," AIAA Paper 72-677, Boston, MA, June 1971.

2. Lomax, H., Bailey, F. R., and Ballhaus, W. F., "On the Numerical Simulation of Three-Dimensional Transonic Flow with Application to the C-141 Wing," NASA TN D-6933, Aug. 1973.

3. Boppe, C. W., "Calculation of Transonic Wing Flows by Grid Embedding," AIAA Paper 77-207, Los Angeles, CA, Jan. 1977.

4. Mason, W., Mackenzie, D. A., Stern, M. A., and Johnson, J. D., "A Numerical Three-Dimensional Viscous Transonic Wing-Body Analysis and Design Tool," AIAA Paper 78-120, Huntsville, AL., Jan. 1978.

5. Jameson, A. and Caughey, D. A., "A Finite Volume Method for Transonic Potential Flow Calculations," AIAA Paper 77-635, Albuquerque, NM, June 1978.

6. Holst, T. L., "A Fast, Conservative Algorithm for Solving the Full-Potential Equation," AIAA Paper 79-1456, Williamsburg, VA, July 1979.

7. Boppe, C. W. and Stern, M. A., "Simulated Transonic Flows for Aircraft with Nacelles, Pylons, and Winglets," AIAA Paper 78-104, Pasadena, CA, Jan. 1980.

8. Caradonna, F. X. and Isom, M. P., "Numerical Calculation of Unsteady Transonic Potential Flow Over Helicopter Rotor Blades," AIAA Journal, Vol. 14, Apr. 1976, pp 482-488.

9. Caradonna, F. X. and Phillippe, J. J., "The Flow Over a Helicopter Blade Tip in the Transonic Regime," Vertica, Vol. 2, 1978, pp 43-60.

10. Borland, C., Rizzetta, D., and Yoshihara, H., "Numerical Solution of Three-Dimensional Unsteady Transonic Flow over Swept Wings," AIAA Paper 80-1369, Snowmass, CO, July 1980.

11. Steger, J. L., and Caradonna, F. X., "A Conservative Implicit Finite Difference Algorithm for the Unsteady Transonic Full Potential Equation," AIAA Paper 80-1368, Snowmass, CO, July 1980.

12. Sankar, N. L., Malone, J. B., and Tassa, Y., "An Implicit Conservative Algorithm for Steady and Unsteady Three-Dimensional Transonic Potential Flows," AIAA Paper 81-1016, Palo Alto, CA, June 1981.

13. Borland, C. J. and Rizzetta, D. P., "Nonlinear Transonic Flutter Analysis," AIAA Paper 81-0608-CP, Atlanta, GA, April 1981.

14. Rizzetta, D. P. and Yoshihara, H., "Computations of the Pitching Oscillation of a NACA 64A-010 Airfoil in the Small Disturbance Limit," AIAA Paper 80-0128, Pasadena, CA,, Jan. 1980.

15. Green, J. E., "Application of Head's Entrainment Method to the Prediction of Turbulent Boundary Layers and Wakes in Compressible Flow," RAE Reports and Memoranda No. 3788, April 1972.

16. Green, J. E., Weeks, D. J., and Brooman, J. W. F., "Prediction of Turbulent Boundary Layers and Wakes in Compressible Flow by a Lag-Entrainment Method," RAE Reports and Memoranda No. 3791, Jan. 1973.

17. East, L. F., Smith, P. D., and Merryman, P. J., "Prediction of the Development of Separated Turbulent Boundary Layers by the Lag-Entrainment Method," RAE Technical Report 77046, Mar. 1977.

18. Wai, J. C. and Yoshihara, H., "Viscous Transonic Flow Over Airfoils," Proceeding of the Seventh International Conference on Numerical Methods in Fluid Dynamics," Palo Alto, CA, June 1980.

19. Wai, J. C. and Yoshihara, H., "Planar Transonic Airfoil Computations with Viscous Interactions," AGARD-CP-291, Sept. 1980.

20. Rizzetta, D. P., "Procedures for the Computation of Unsteady Transonic Flows Including Viscous Effects," NASA CR-166249, Aug. 1981.

21. Mason, W. H., Ballhaus, W. F., Mackenzie, C., Frick, J., and Stern, M., "An Automated Procedure for Computing the Three-Dimensional Transonic Flow over Wing-Body Combinations, Including Viscous Effects," AFFDL-TR-77-122, Vol. I., Feb. 1977.

22. Rizzetta, D. P. and Yoshihara, H., "Oscillating Supercritical Airfoils in the Transonic Regime with Viscous Interactions," AGARD-CP-296, Sept. 1980.

23. Bradshaw, P., Ferriss, D. H., and Atwell, N. P., "Calculation of Turbulent Boundary-Layer Development Using the Turbulent Energy Equation," Journal of Fluid Mechanics, Vol. 28, 1967, pp 593-616.

24. Head, M. R., "Entrainment in the Turbulent Boundary Layer," ARC Reports and Memoranda No. 3152, 1958.

25. Borland, C. J. and Rizzetta, D. P., "Transonic Unsteady Aerodynamics for Aeroelastic Applications--Vol I: Technical Development Summary," AFFWAL TR-80-3107, Vol. I, June 1982.

26. Borland, C. J., Thorne, R. G., and Yeagley, L. R., "Transonic Unsteady Aerodynamics for Aeroelastic Application--Vol. II: User's Manual," AFFWAL TR-80-3107, Vol. II, June 1982.

27. Thorne, R. G. and Yeagley, L. R., "Transonic Unsteady Aerodynamics for Aeroelastic Applications--Vol. III: Programmer's Manual," AFFWAL TR-80-3107, Vol. III, June 1982.

28. Schlichting, H., Boundary Layer Theory, McGraw-Hill Book Company Inc., New York, 1960, pp 536-537.

29. Hinson, B. L. and Burdges, K. P., "Acquisition and Application of Transonic Wing and Far-Field Test Data for Three-Dimensional Computational Method Evaluation--Volume I," AFSOR-TR-80-0421, Mar. 1980.

30. Hinson, B. L. and Burdges, K. P., "Acquisition for Application of Transonic Wing and Far-Field Test Data for Three-Dimensional Computational Method Evaluation--Volume II," AFSOR-TR-80-0422, Mar. 1980.

31. Rizzetta, D. P. and Borland, C. J., "Unsteady Transonic Flow over Wings Including Inviscid/Viscous Interaction, AIAA Journal, Vol. 21, No. 3, March 1983, pp 363-371.

32. Streett, C. L., "Viscous-Inviscid Interaction for Transonic Wing-Body Configurations Including Wake Effects," AIAA Paper 81-1266, Palo Alto, CA, June 1981.

33. Bland, S. R., "AGARD Two-Dimensional Aeroelastic Configurations," AGARD-AR-156, Aug. 1979.

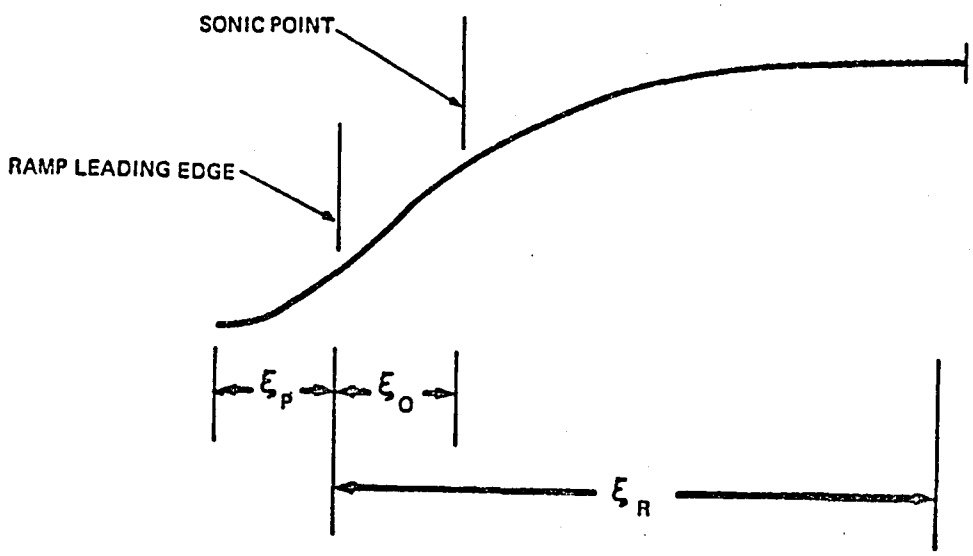

Figure 1. Viscous Ramp Geometry

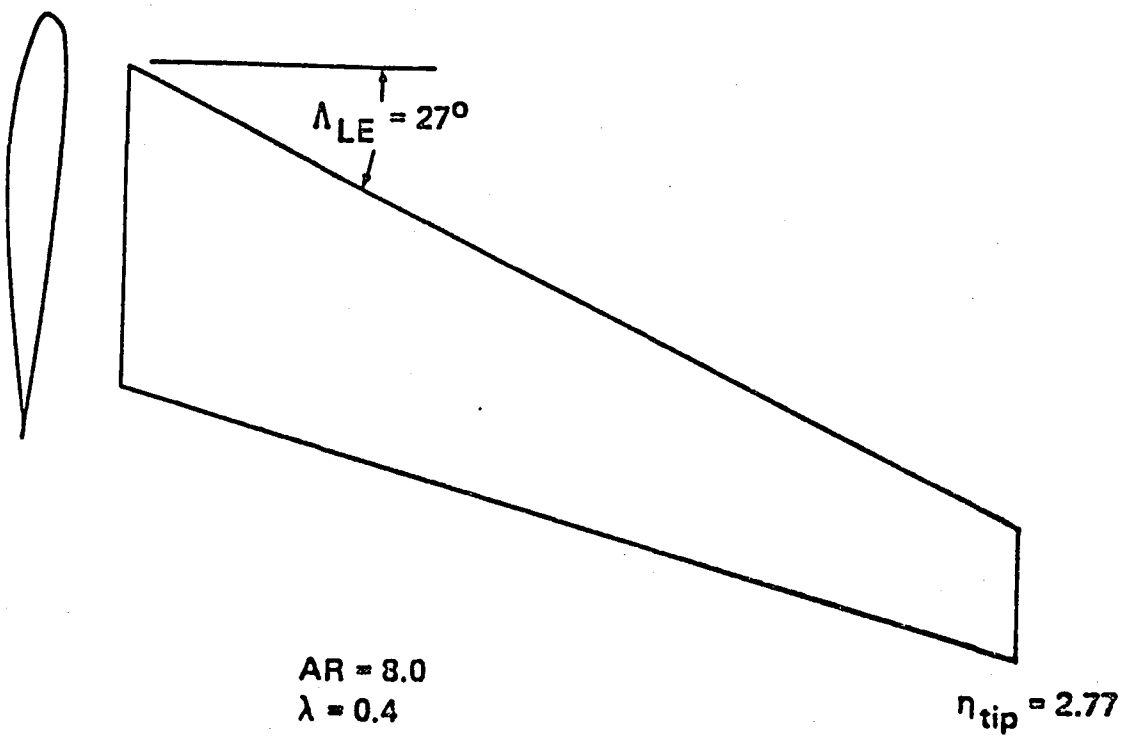

Figure 2. Lockheed - Georgia "Wing A"

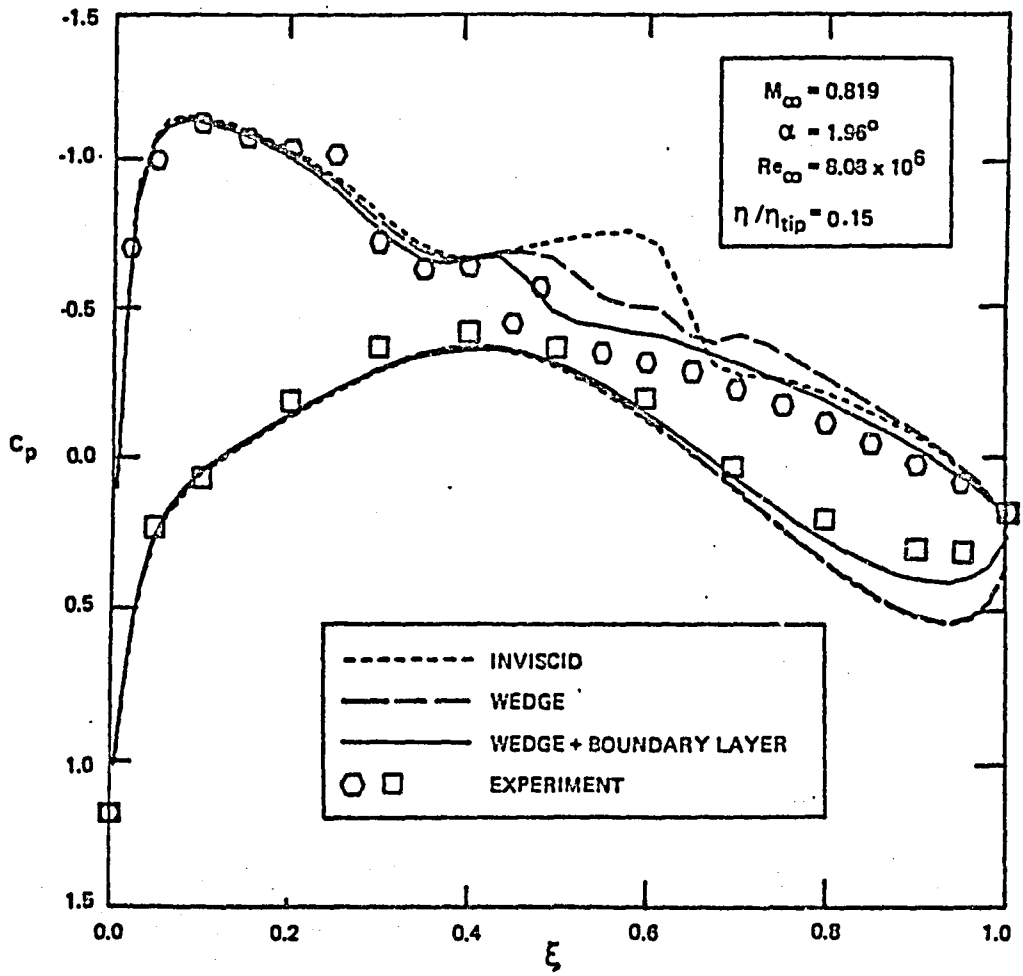

Figure 3 a. Steady Surface Pressure Distributions for Lockheed "Wing A" at $\eta/\eta_{tip} = 0.15$

ORIGINAL PAGE IS
OF POOR QUALITY

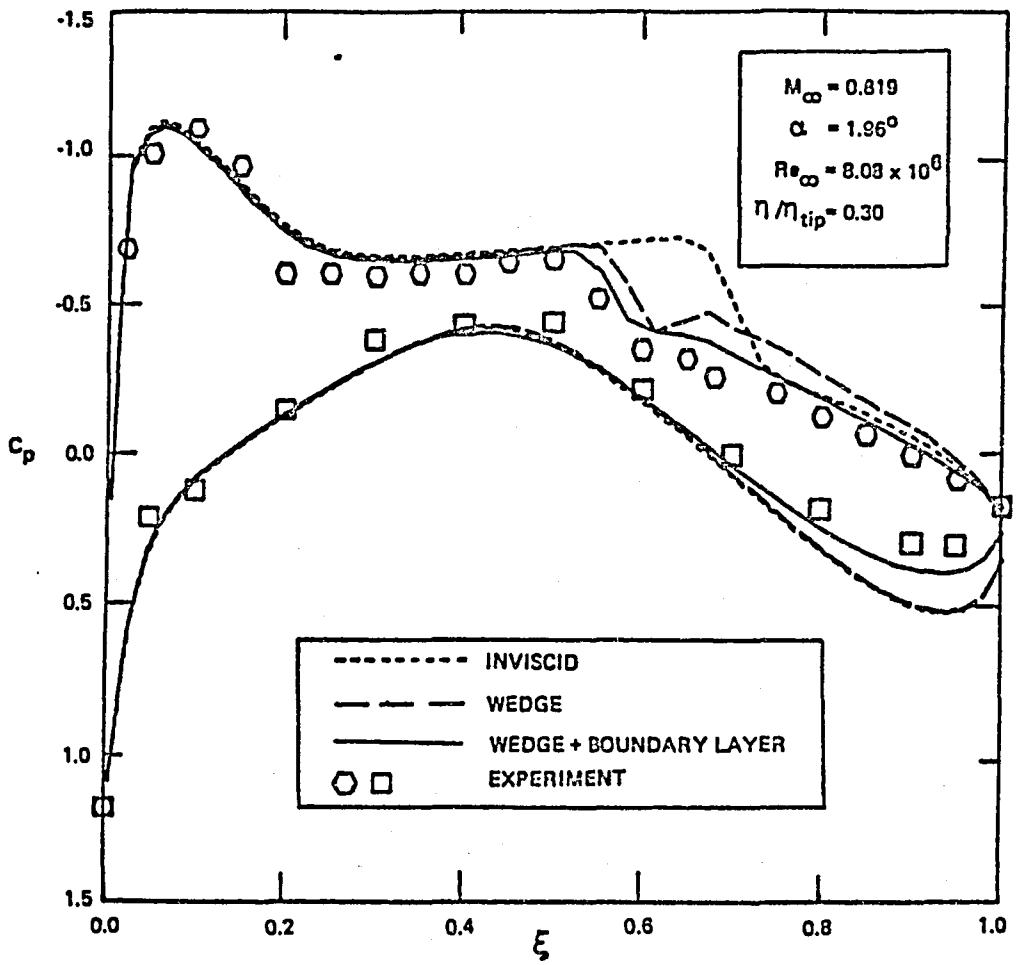

Figure 3 b. Steady Surface Pressure Distributions for Lockheed "Wing A" at η/η_{tip} = 0.30

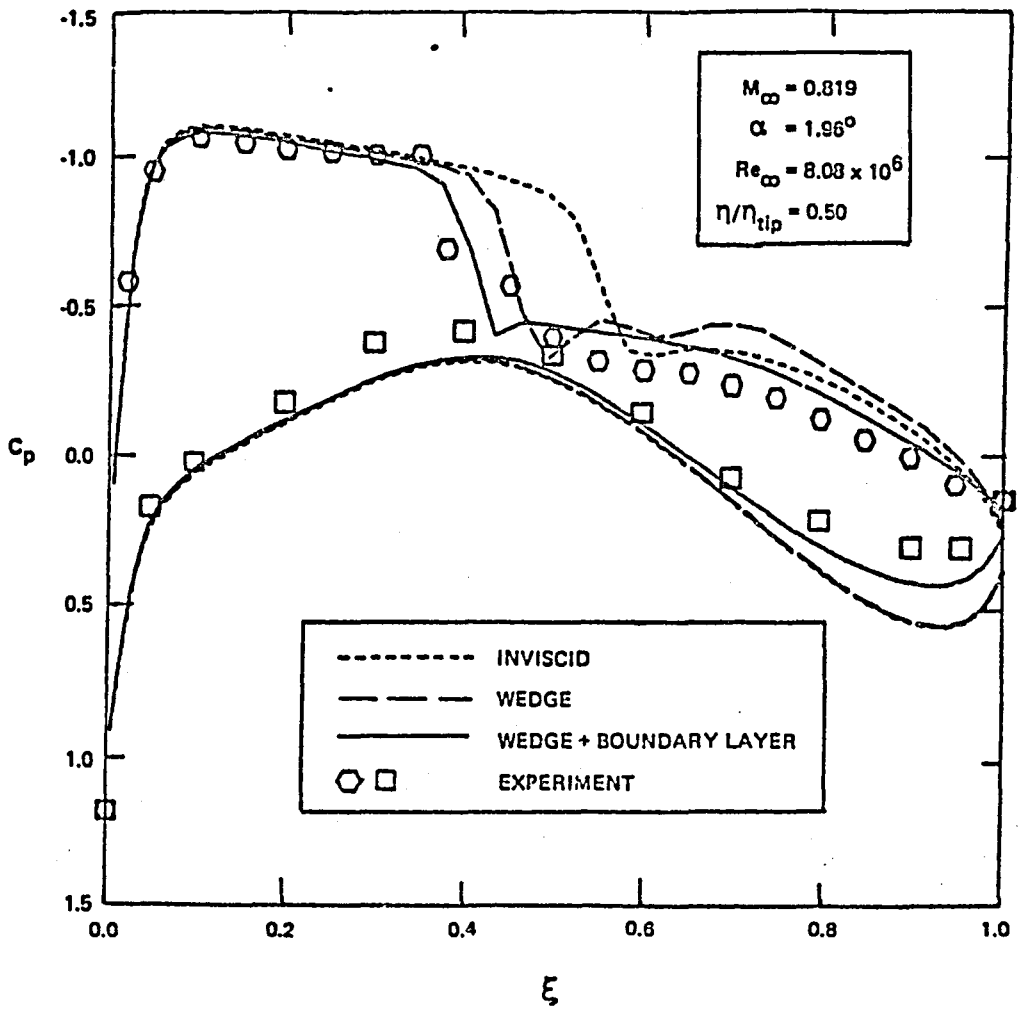

Figure 3 c. Steady Surface Pressure Distributions for Lockheed "Wing A" at $\eta/\eta_{tip} = 0.50$

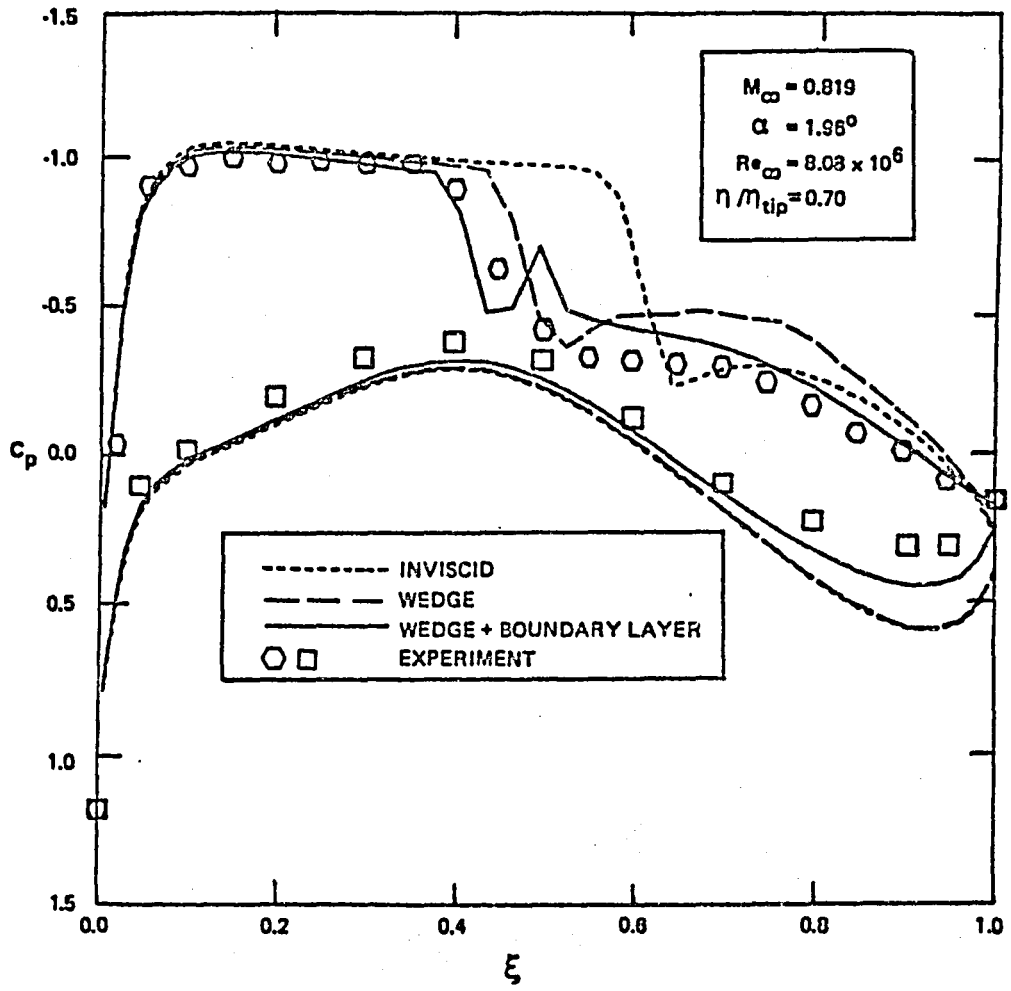

Figure 3 d. Steady Surface Pressure Distributions for Lockheed "Wing A" at $\eta/\eta_{tip} = 0.70$

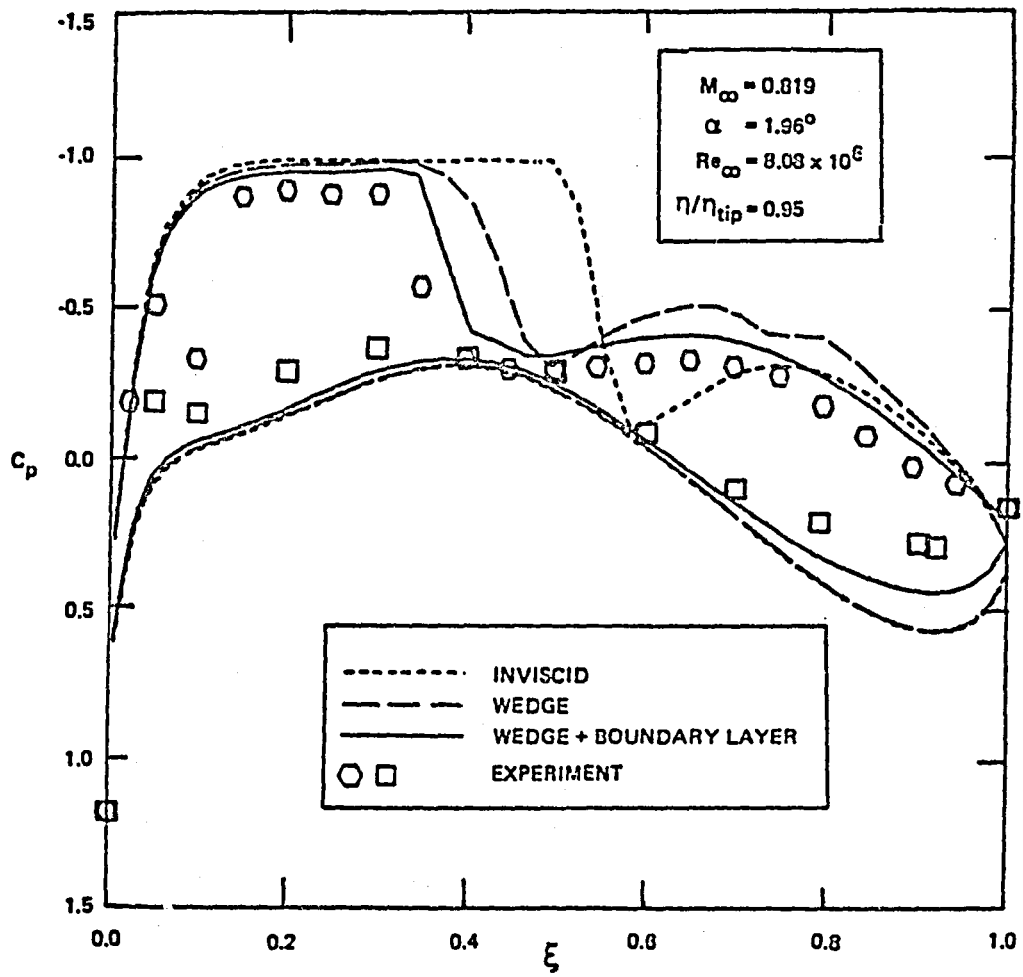

Figure 3 e. Steady Surface Pressure Distributions for Lockheed "Wing A" at $\eta/\eta_{tip} = 0.95$

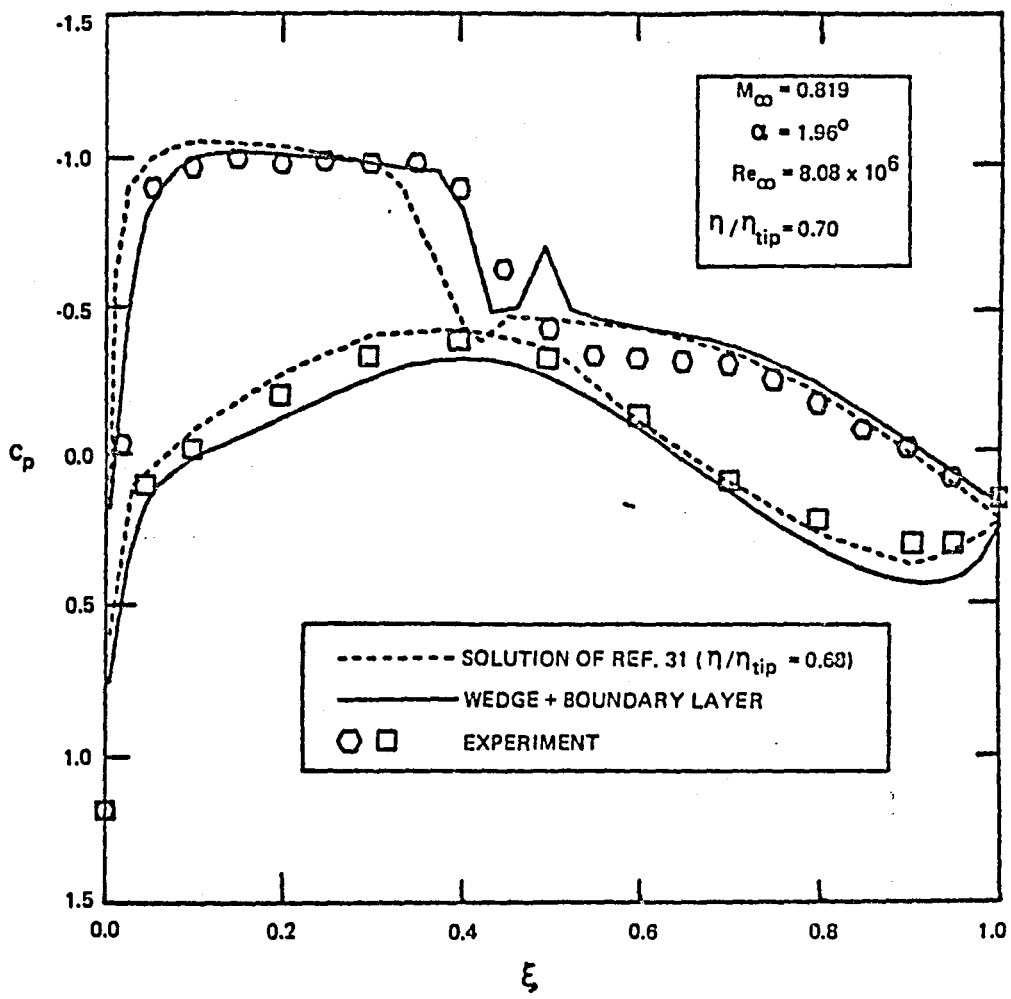

Figure 4. Steady Surface Pressure Distribution for Lockheed "Wing A" at $\eta/\eta_{tip} = 0.70$

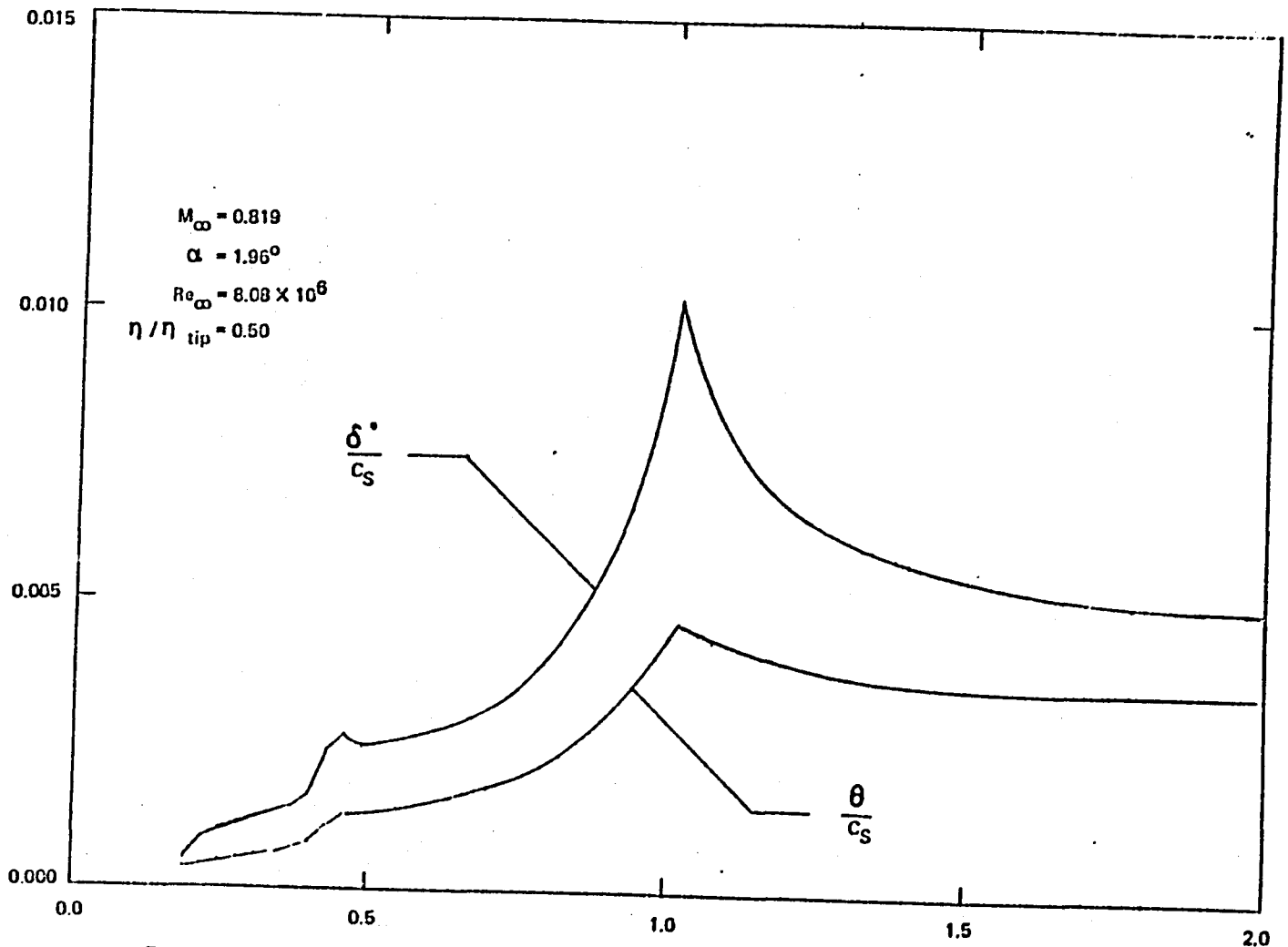

Figure 5. Steady Upper Surface Displacement and Momentum Defect Thickness Distributions for Lockheed "Wing A" at $\eta/\eta_{tip} = 0.50$

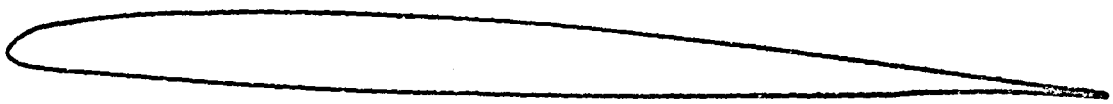

Figure 6. MBB-A3 Airfoil Section

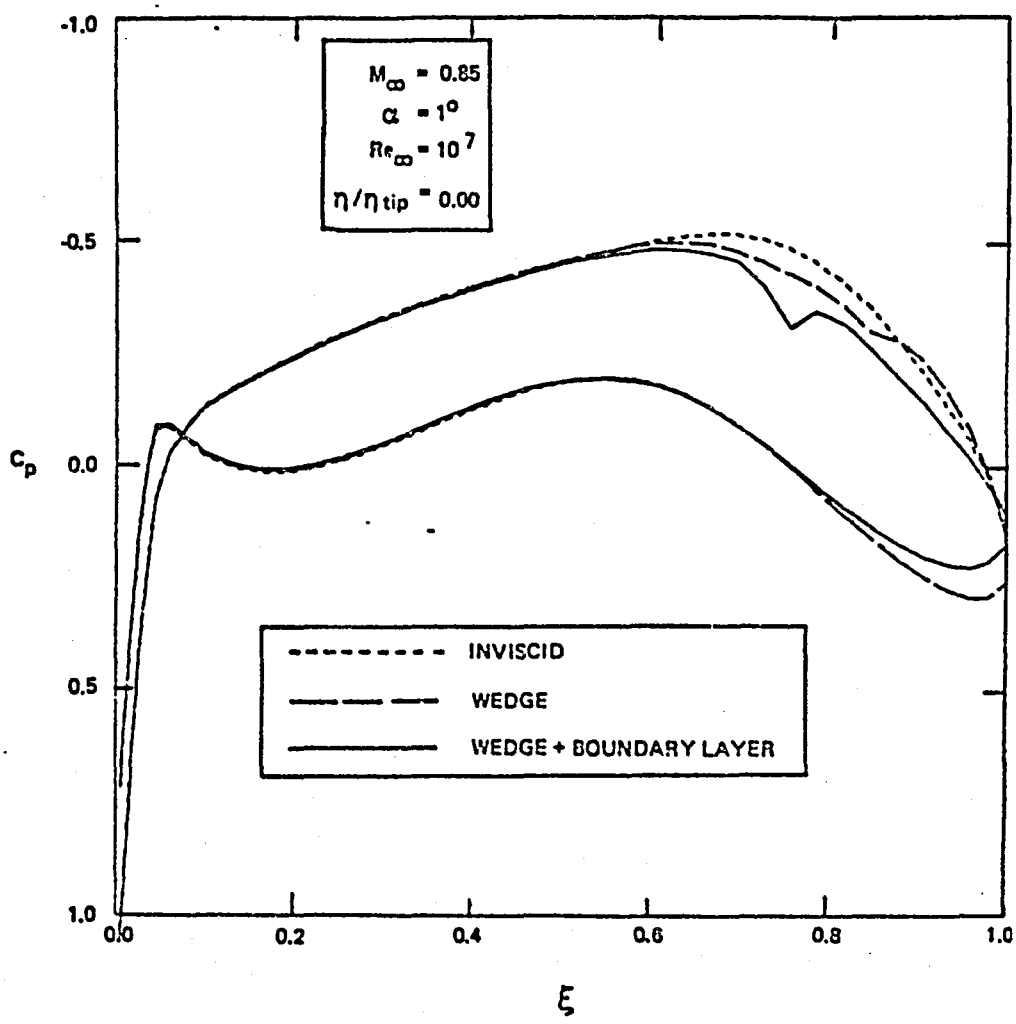

Figure 7a. Steady Surface Pressure Distributions for MBB-A3 Wing at $\eta/\eta_{tip} = 0.00$

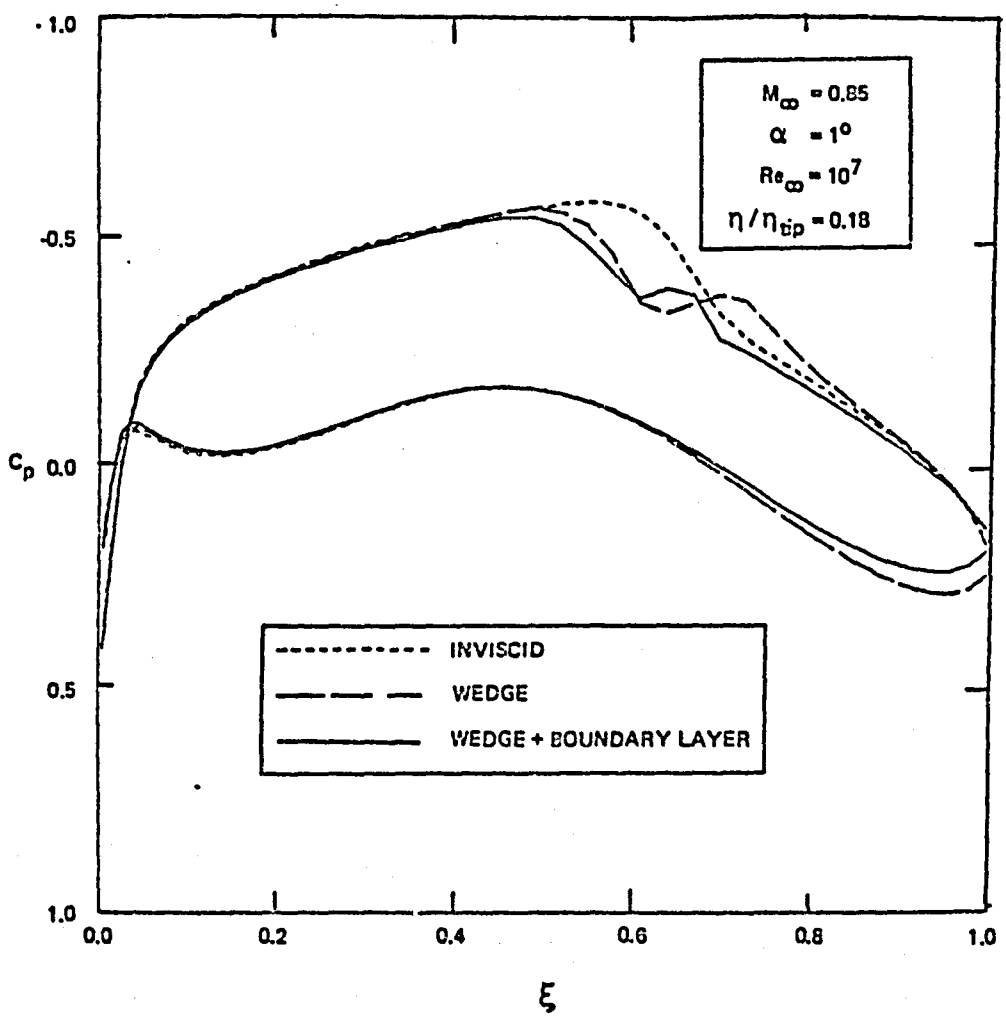

Figure 7 b. Steady Surface Pressure Distributions for MBB-A3 Wing at η/η_{tip} = 0.18

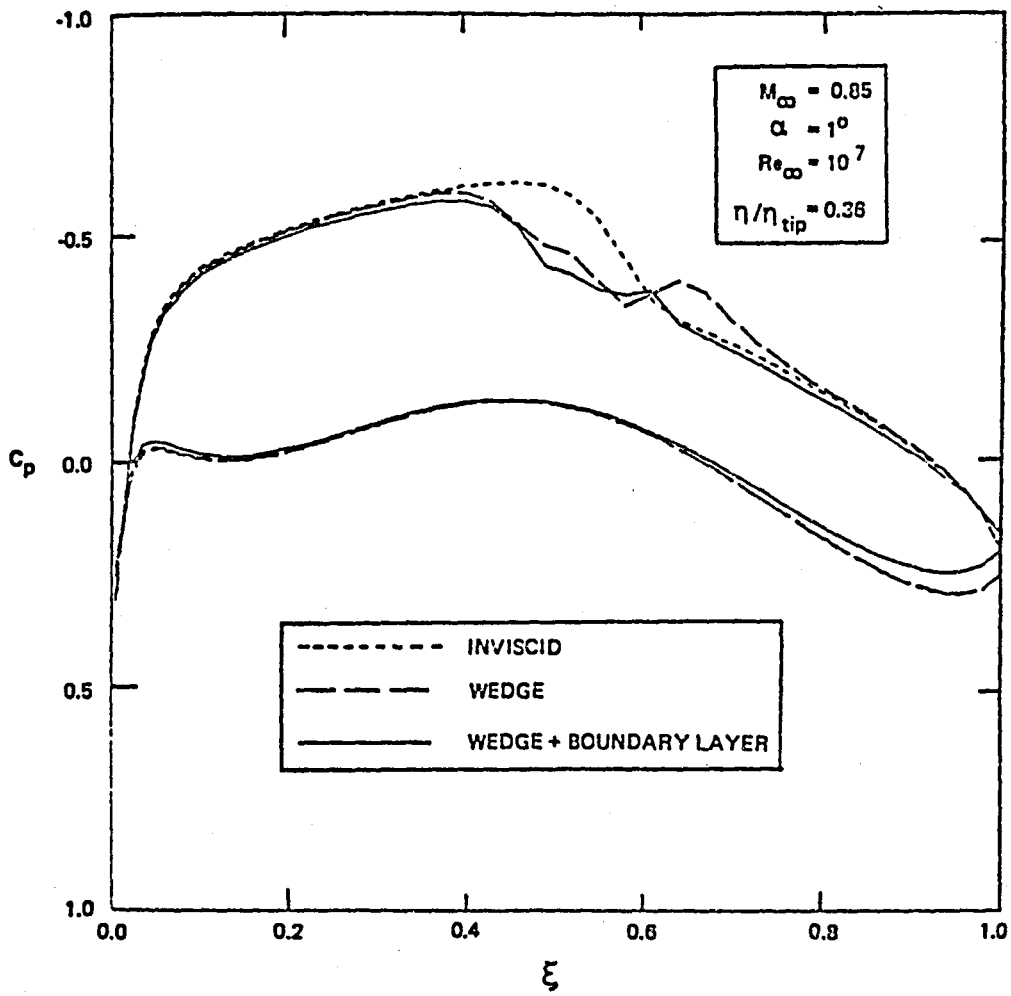

Figure 7 c. Steady Surface Pressure Distributions for MBB-A3 Wing at $\eta/\eta_{tip} = 0.36$

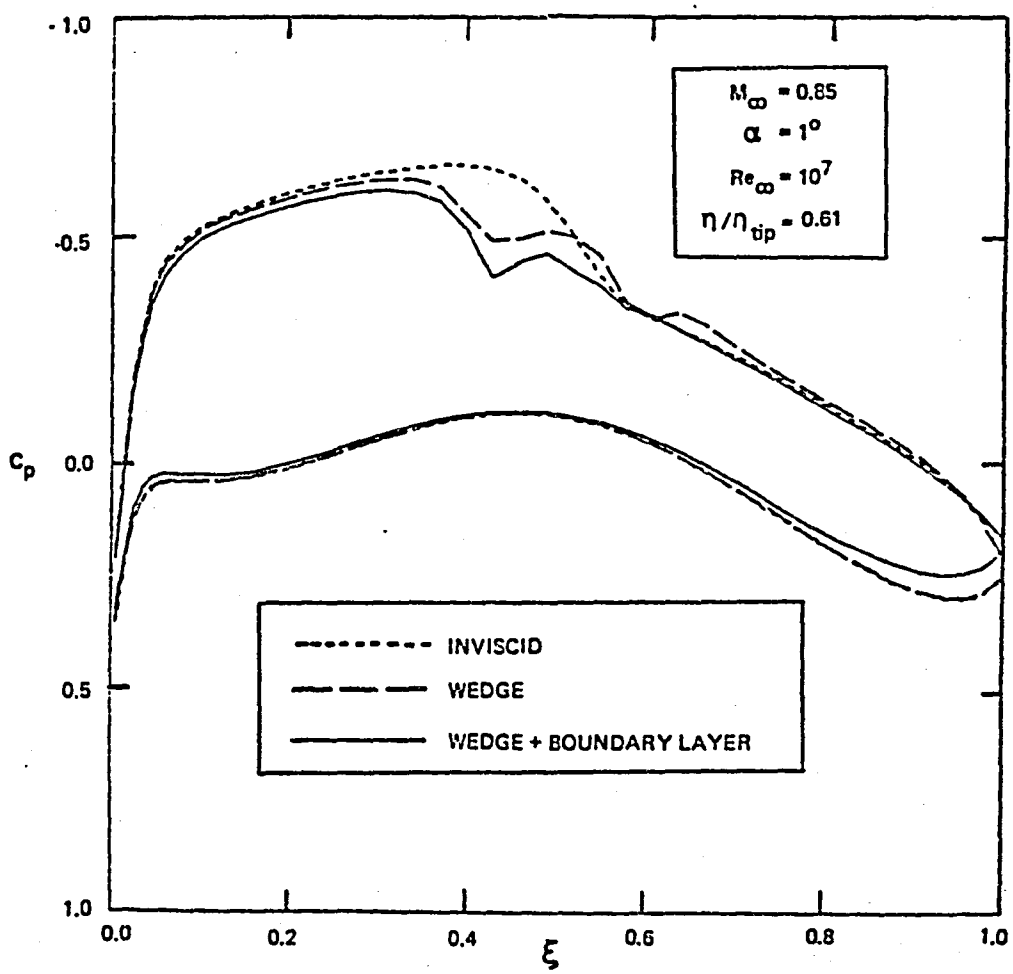

Figure 7d. Steady Surface Pressure Distributions for MBB-A3 Wing at $\eta / \eta_{tip} = 0.61$

ORIGINAL PAGE IS
OF POOR QUALITY

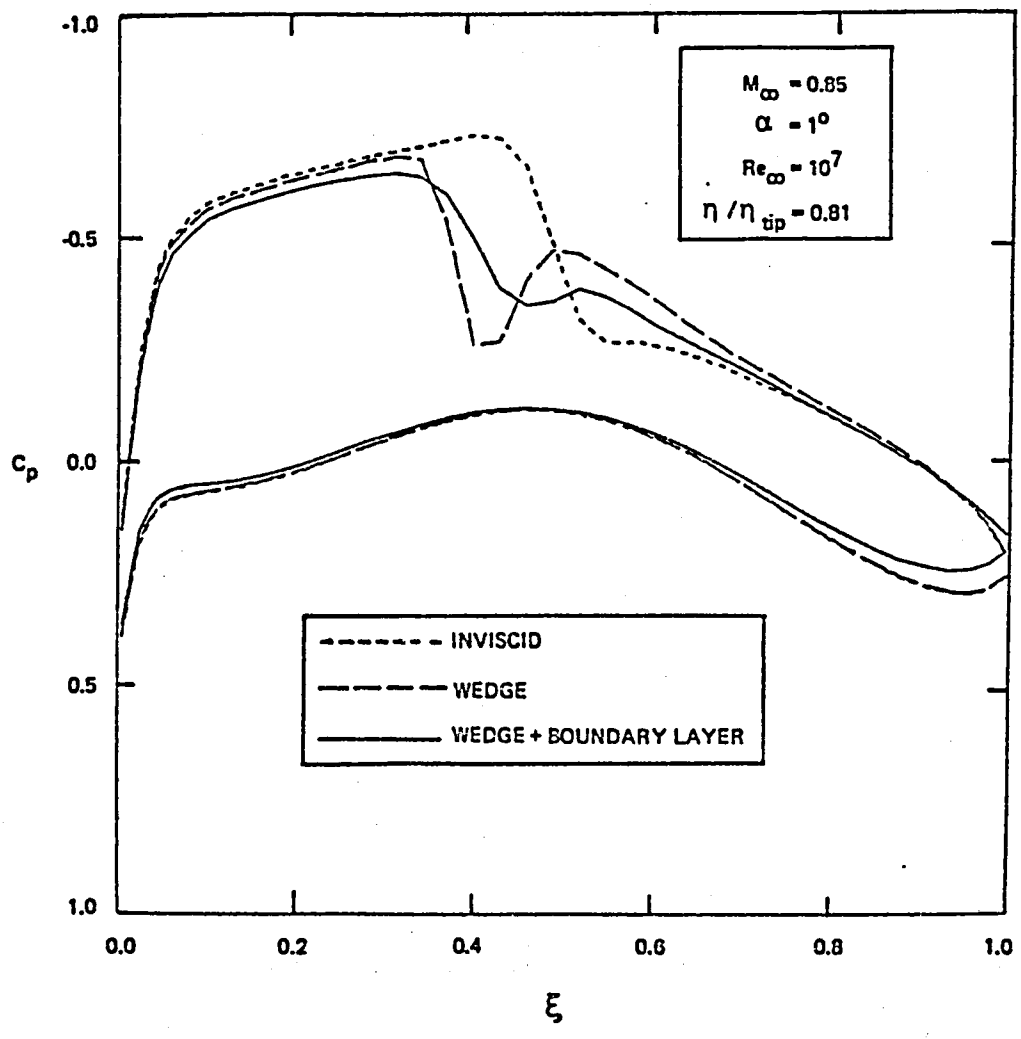

Figure 7e. Steady Surface Pressure Distributions for MBB-A3 Wing at $\eta/\eta_{tip} = 0.81$

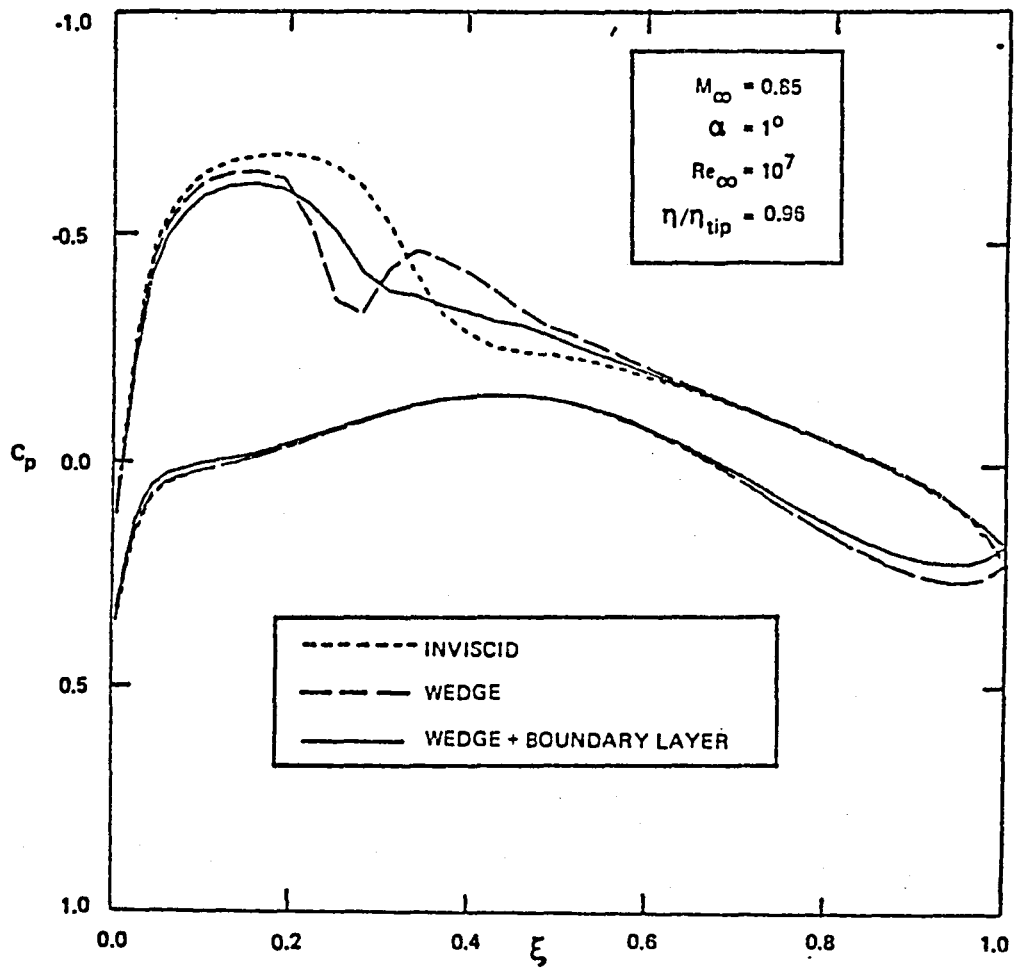

Figure 7 f. Steady Surface Pressure Distributions for MBB-A3 Wing at $\eta/\eta_{tip} = 0.96$

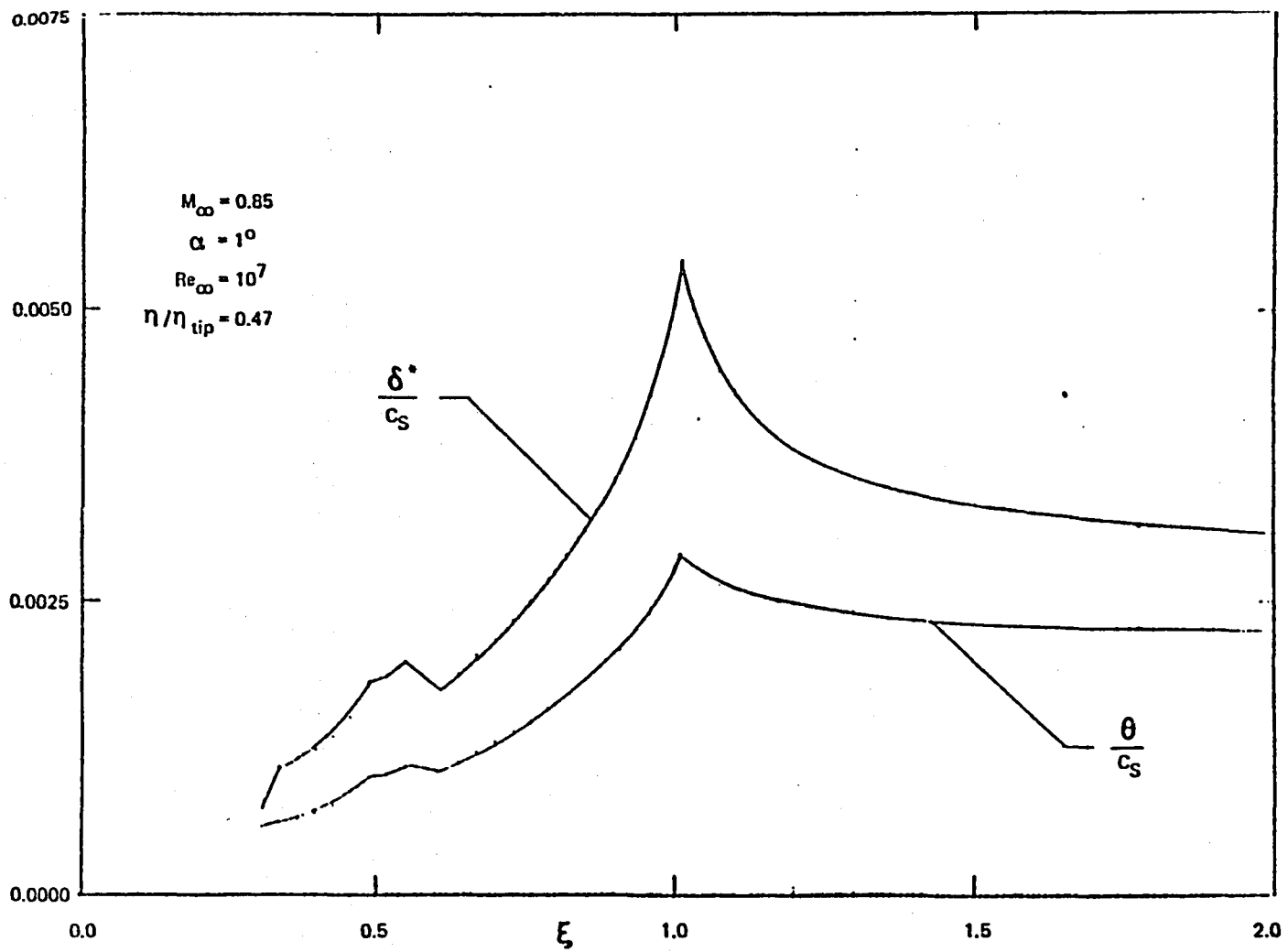

Figure 8. Steady Upper Surface Displacement and Momentum Defect Thickness Distributions for MBB-A3 Wing at $\eta/\eta_{tip} = 0.47$

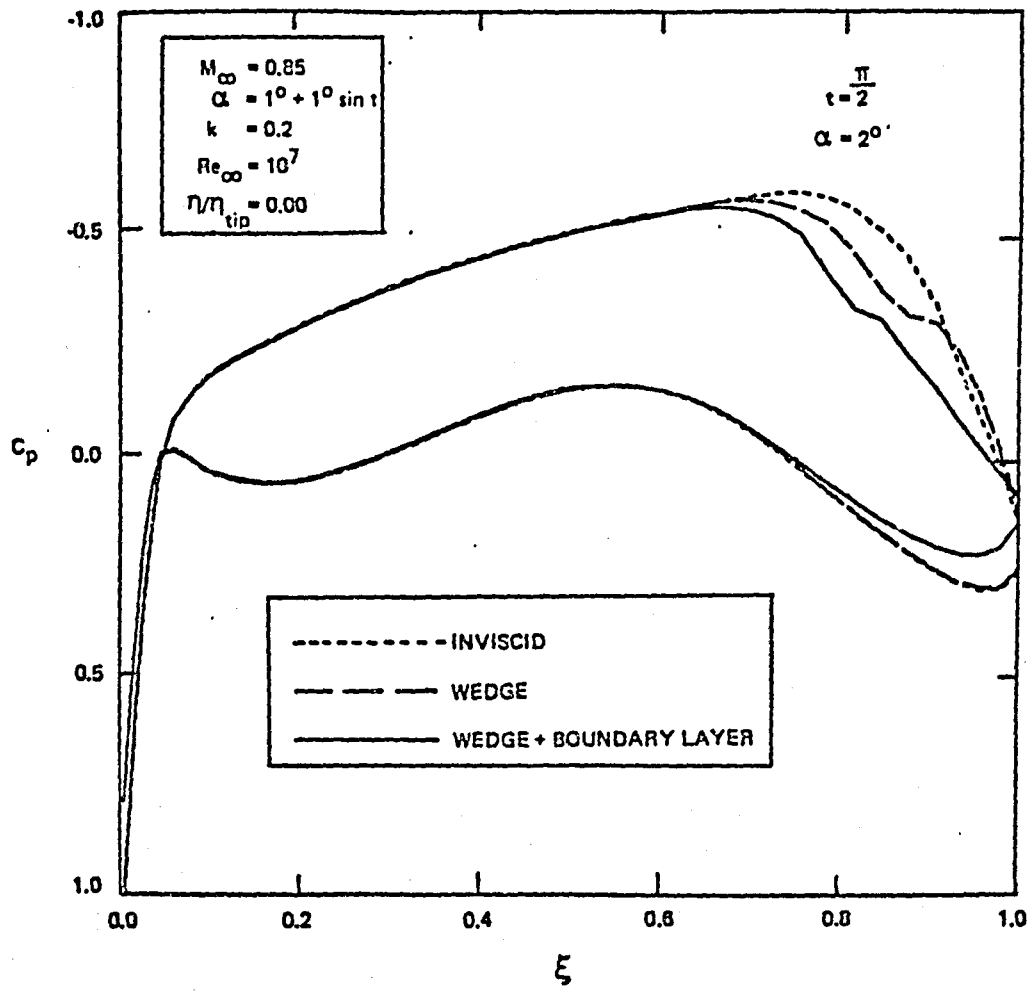

Figure 9 a. Unsteady Surface Pressure Distributions for MBB-A3 Wing at η/η_{tip} = 0.00, $t\,\frac{\pi}{2}$, $\alpha = 2°$

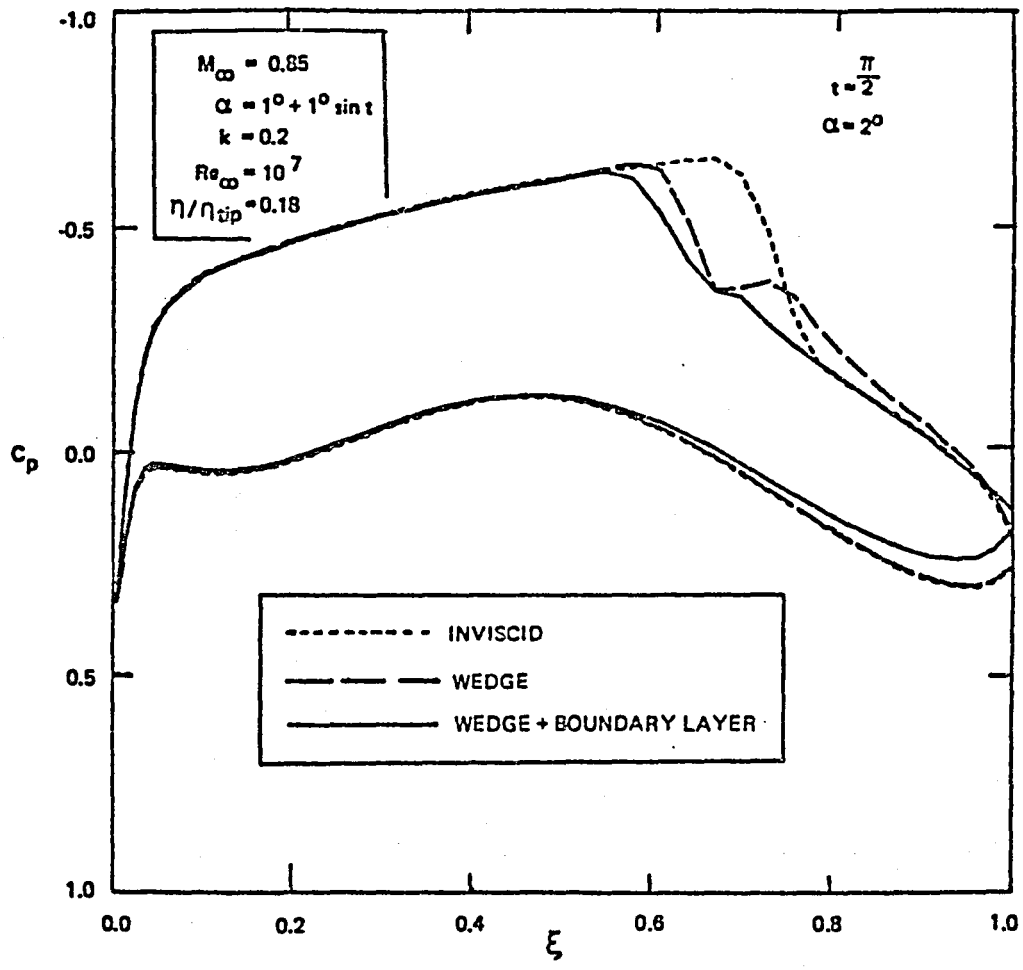

Figure 9b. Unsteady Surface Pressure Distributions for MBB-A3 Wing at $\eta/\eta_{tip} = 0.18$, $t = \frac{\pi}{2}$, $\alpha = 2^o$

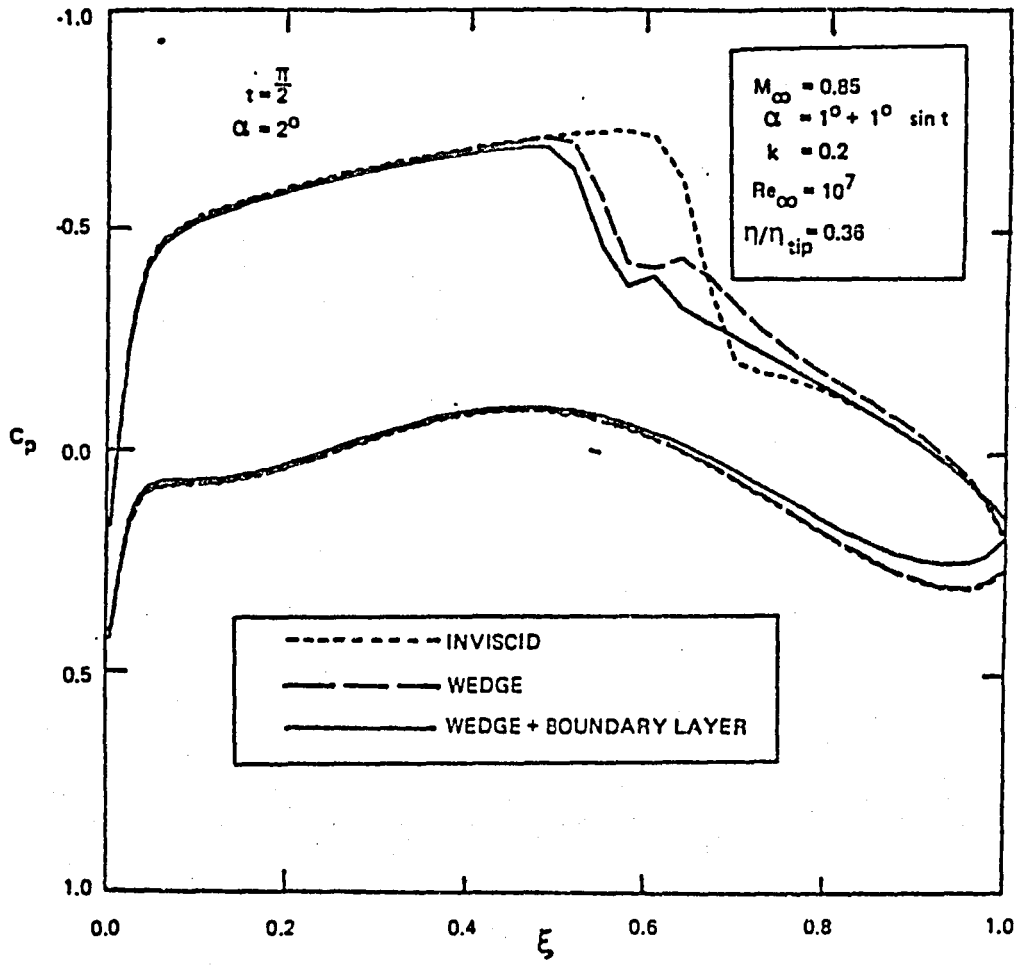

Figure 9 c. Unsteady Surface Pressure Distributions for MBB-A3 Wing at $\eta/\eta_{tip} = 0.36$, $t = \frac{\pi}{2}$, $\alpha = 2^o$

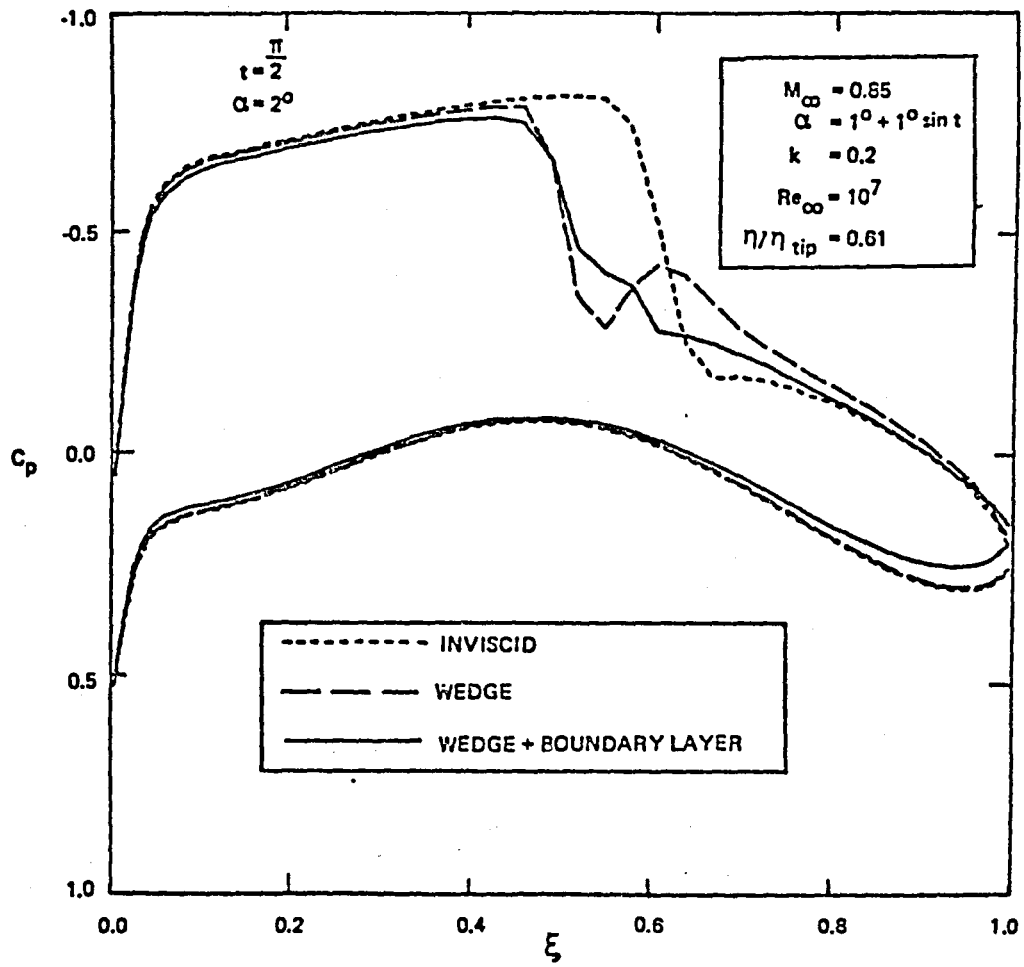

Figure 9 d. Unsteady Surface Pressure Distributions for MBB - A3 Wing at $\eta/\eta_{tip} = 0.61$, $t = \frac{\pi}{2}$, $\alpha = 2^o$

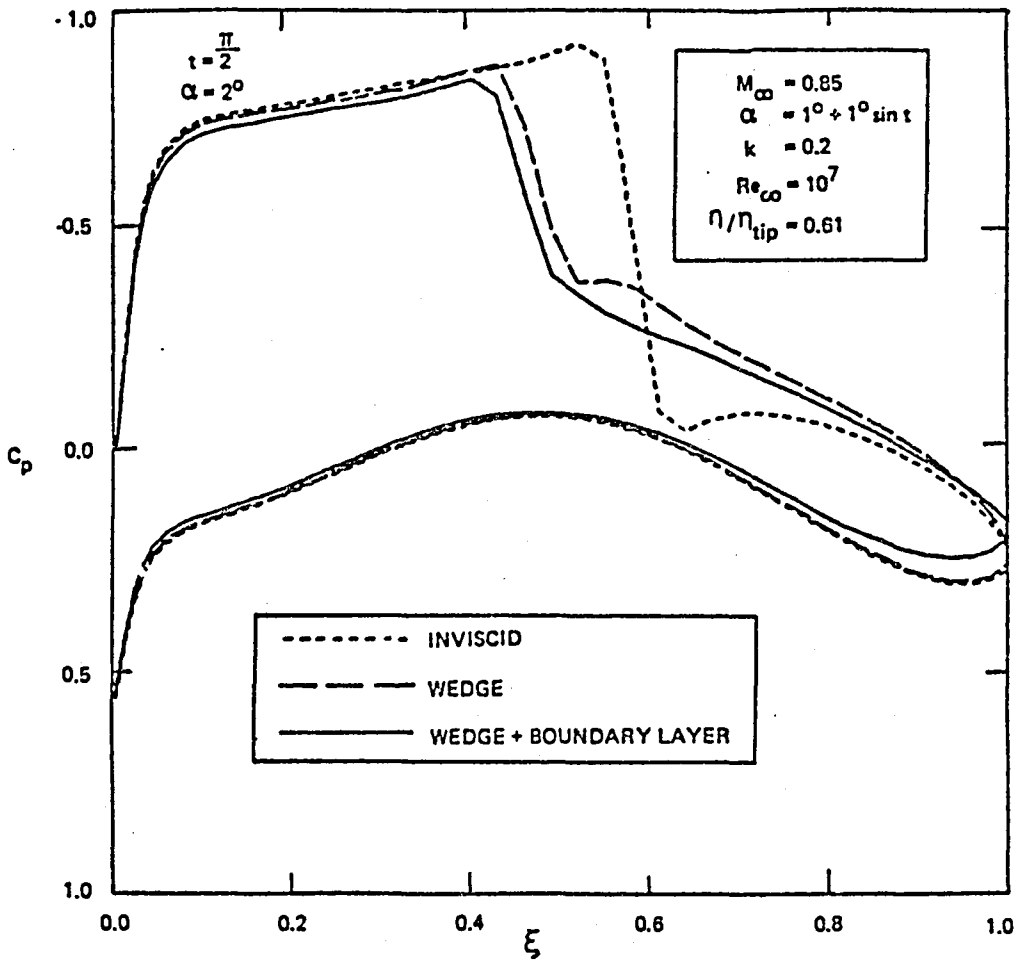

Figure 9 e. Unsteady Surface Pressure Distributions for MBB-A3 Wing at $\eta/\eta_{tip} = 0.81$, $t = \frac{\pi}{2}$, $\alpha = 2^o$

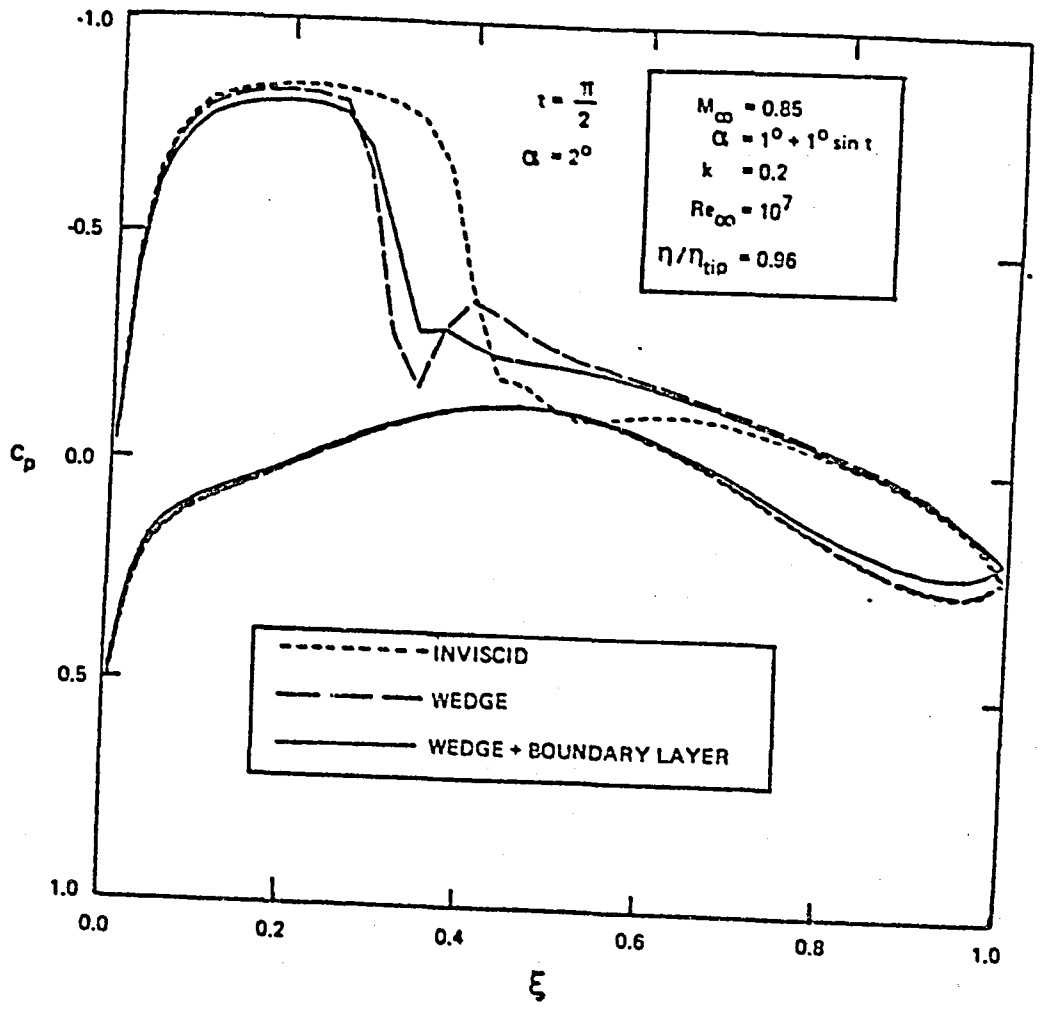

Figure 9 f. Unsteady Surface Pressure Distributions for MBB-A3 Wing at $\eta/\eta_{tip} = 0.96$, $t = \frac{\pi}{2}$, $\alpha = 2^o$

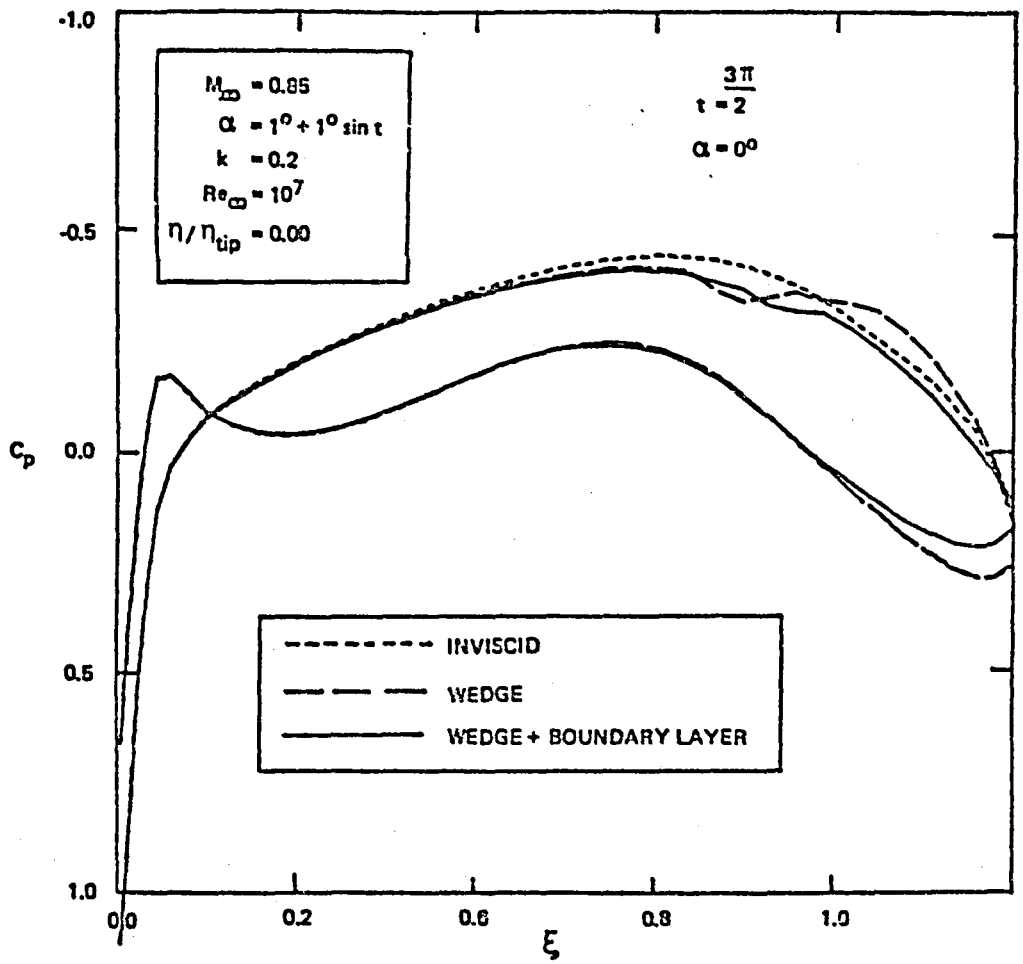

Figure 10 a. Unsteady Surface Pressure Distriubtions for MBB-A3 Wing at $\eta/\eta_{tip} = 0.00$, $t = \frac{3\pi}{2}$, $\alpha = 0^o$

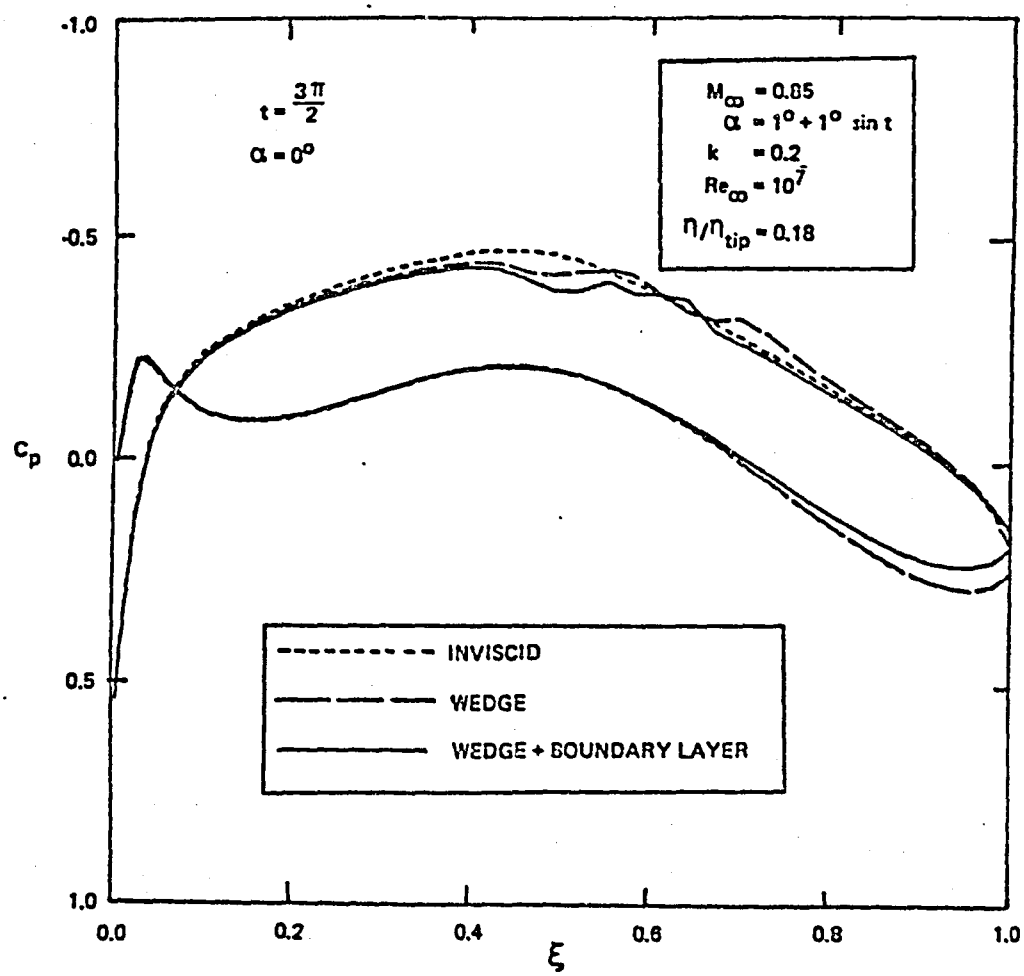

Figure 10 b. Unsteady Surface Pressure Distributions for MBB-A3 Wing at $\eta/\eta_{tip} = 0.18$, $t = \frac{3\pi}{2}$, $\alpha = 0^o$

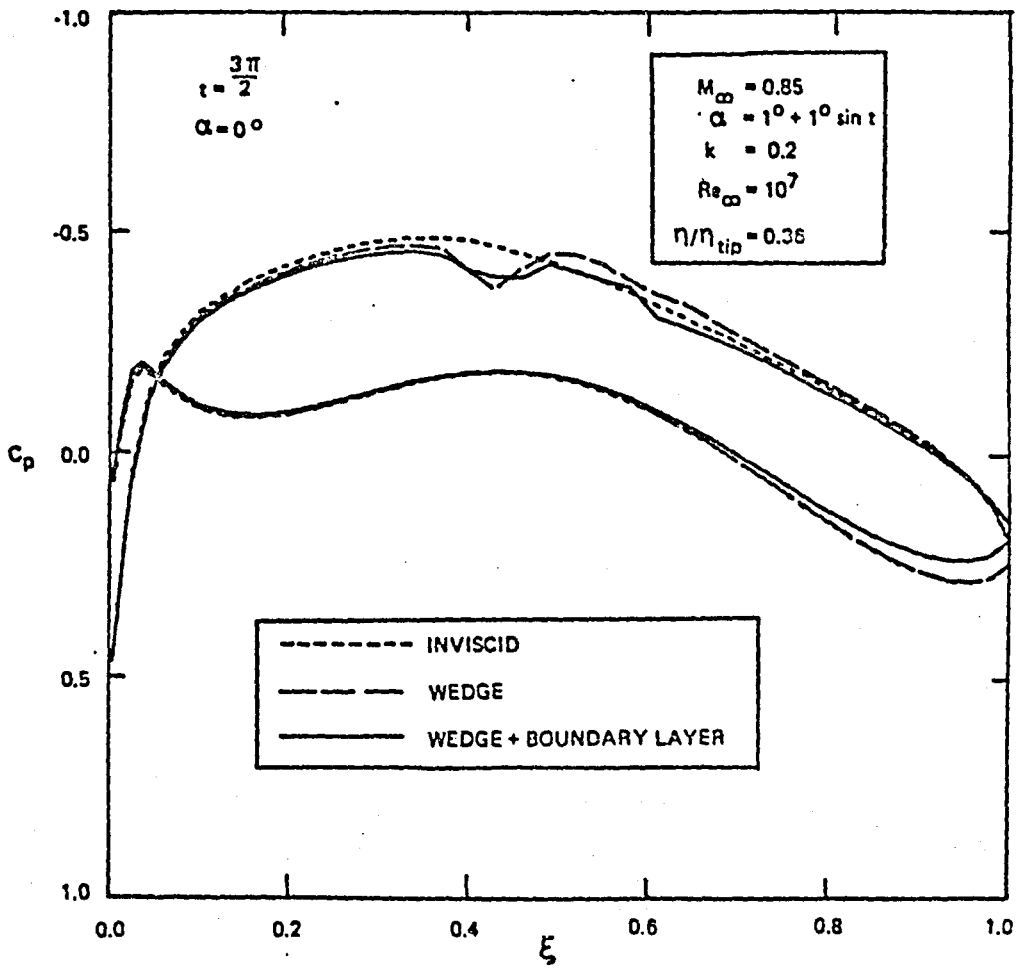

Figure 10 c. Unsteady Surface Pressure Distributions for MBB-A3 Wing at $\eta / \eta_{tip} = 0.36$, $t = \frac{3\pi}{2}, = 0^0$

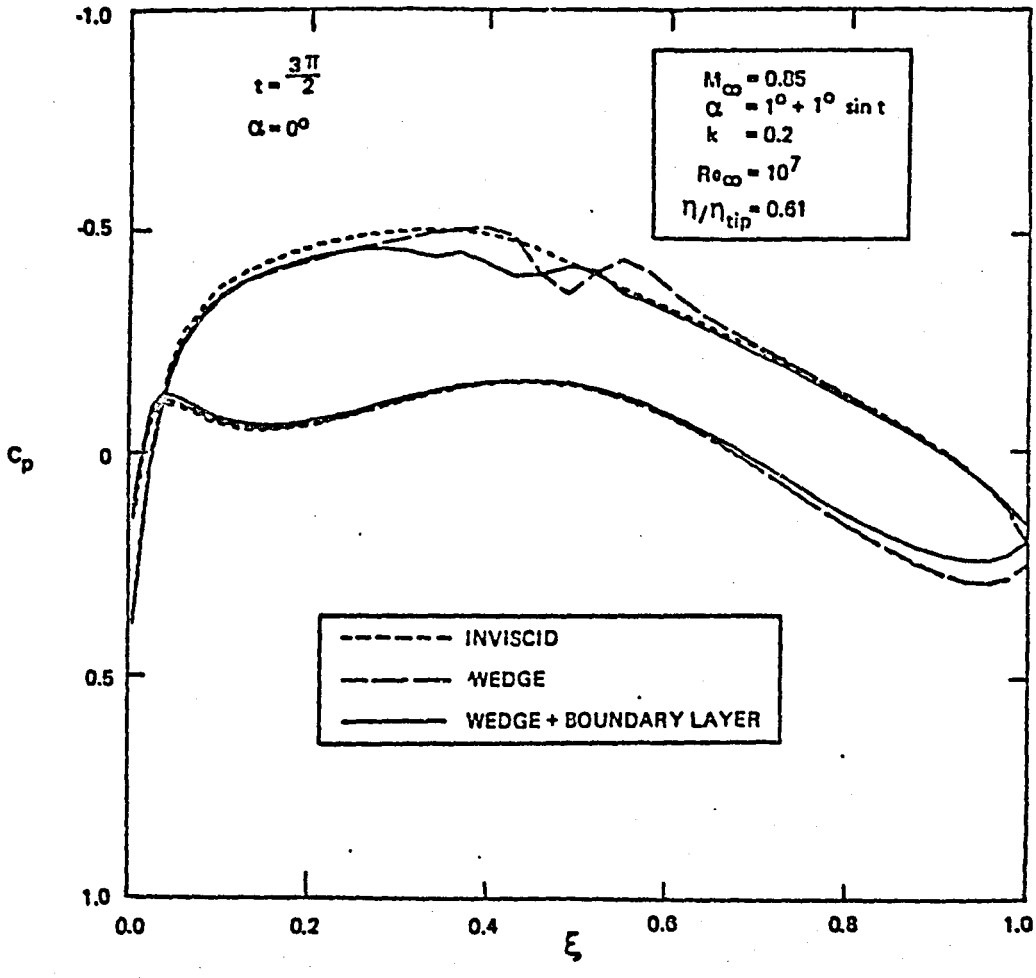

Figure 10 d. Unsteady Surface Pressure Distributions for MBB-A3 Wing at $\eta/\eta_{tip} = 0.61$, $t = \frac{3\pi}{2}$, $= 0^o$

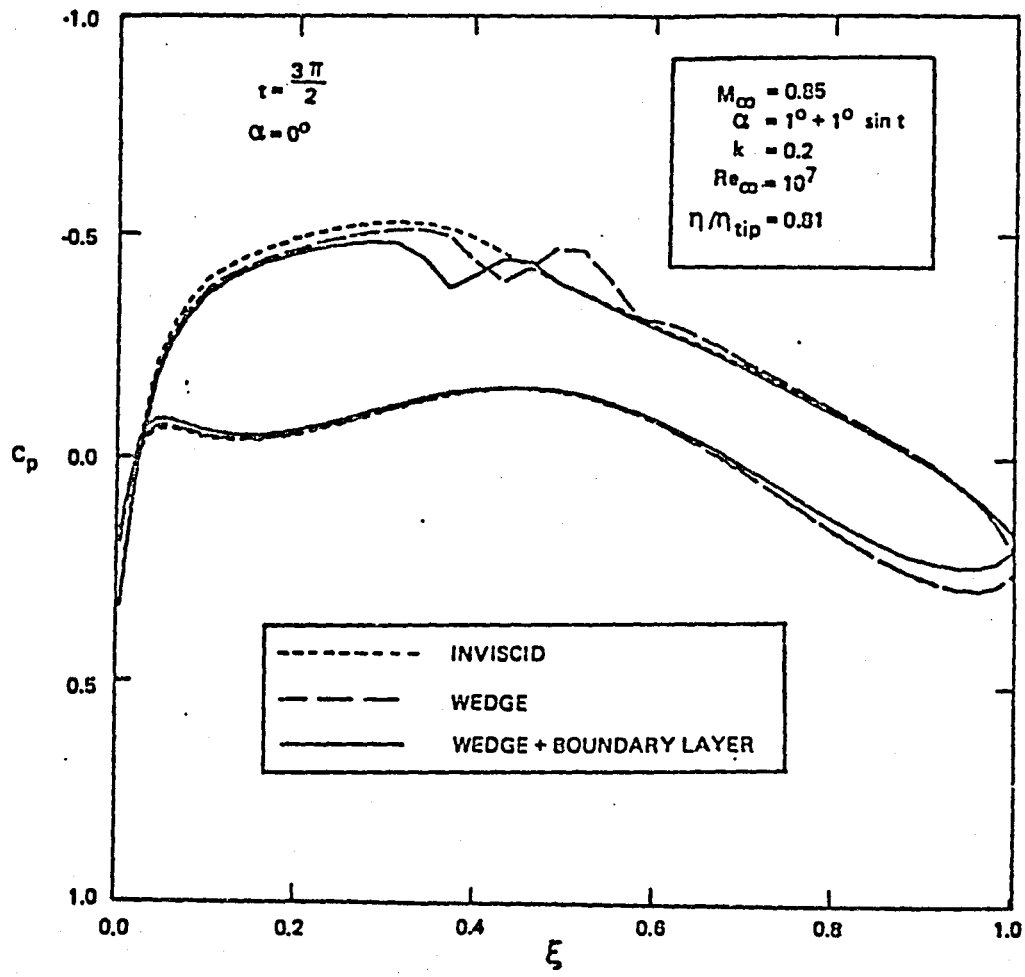

Figure 10 e. Unsteady Surface Pressure Distributions for MBB-A3 Wing at $\eta/\eta_{tip} = 0.81$, $t = \frac{3\pi}{2}$, $\alpha = 0^o$

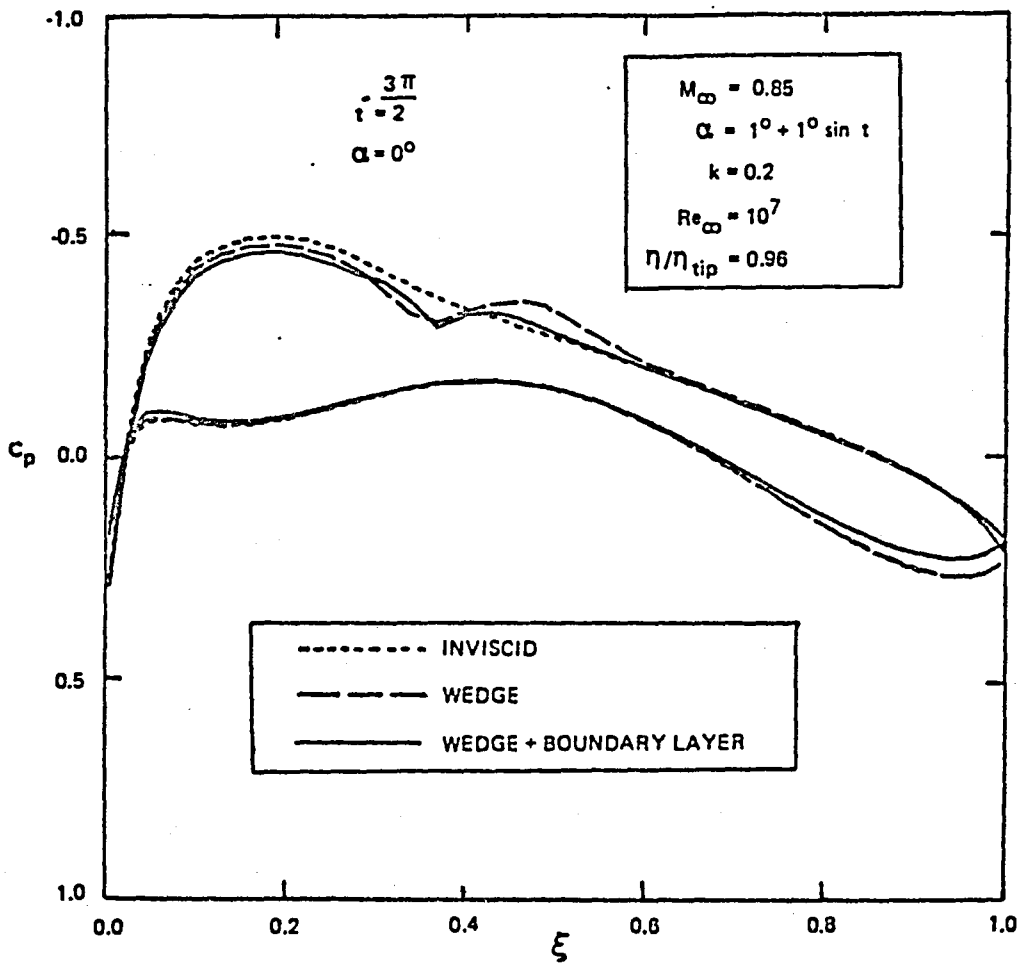

Figure 10f. Unsteady Surface Pressure Distributions ofr MBB-A3 Wing at $\eta/\eta_{tip} = 0.96$,

$t = \frac{3\pi}{2}$, $\alpha = 0^o$

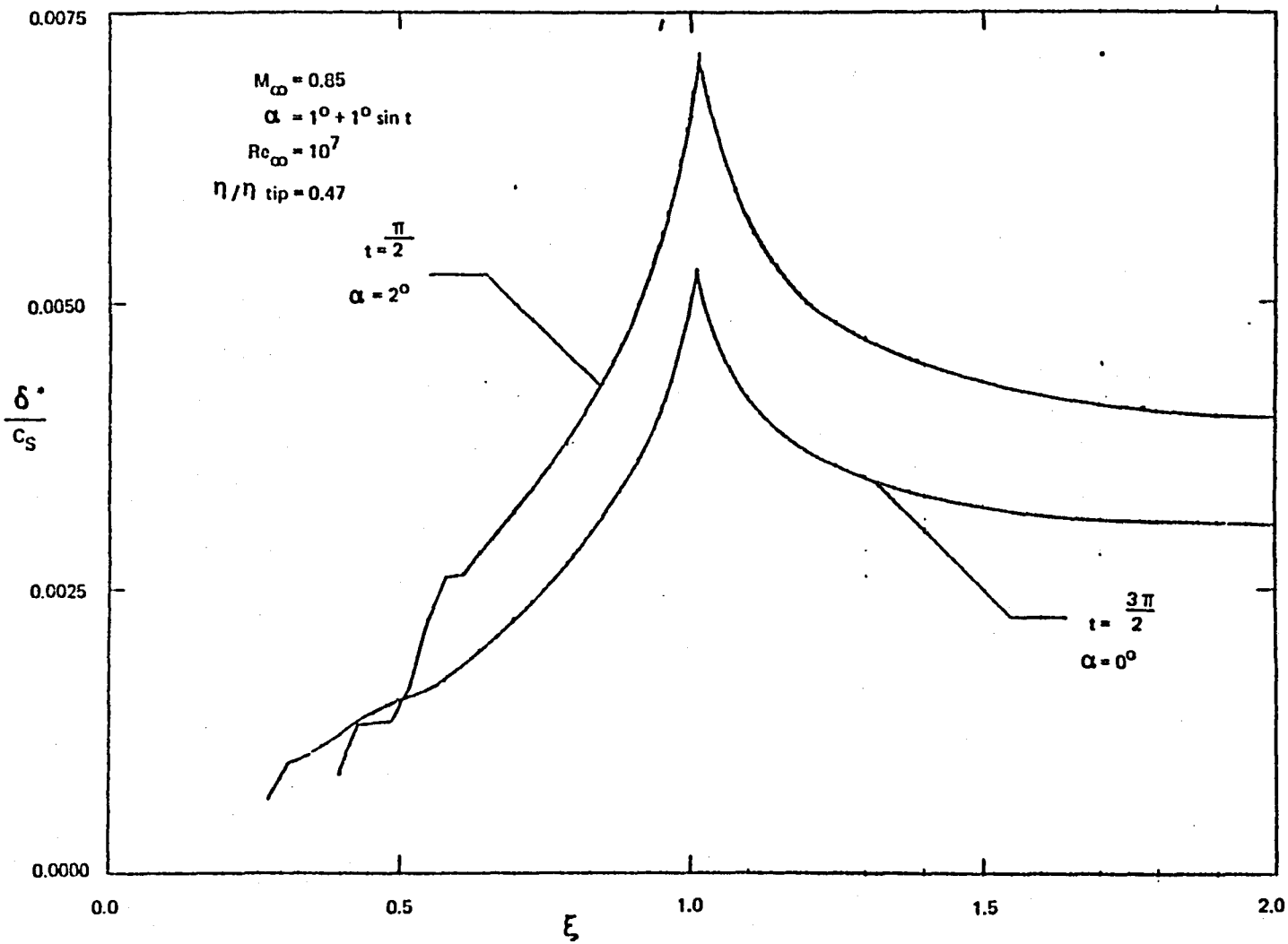

Figure 11. Unsteady Upper Surface Displacement Thickness Distributions for MBB-A3 Wing at $\eta/\eta_{tip} = 0.47$

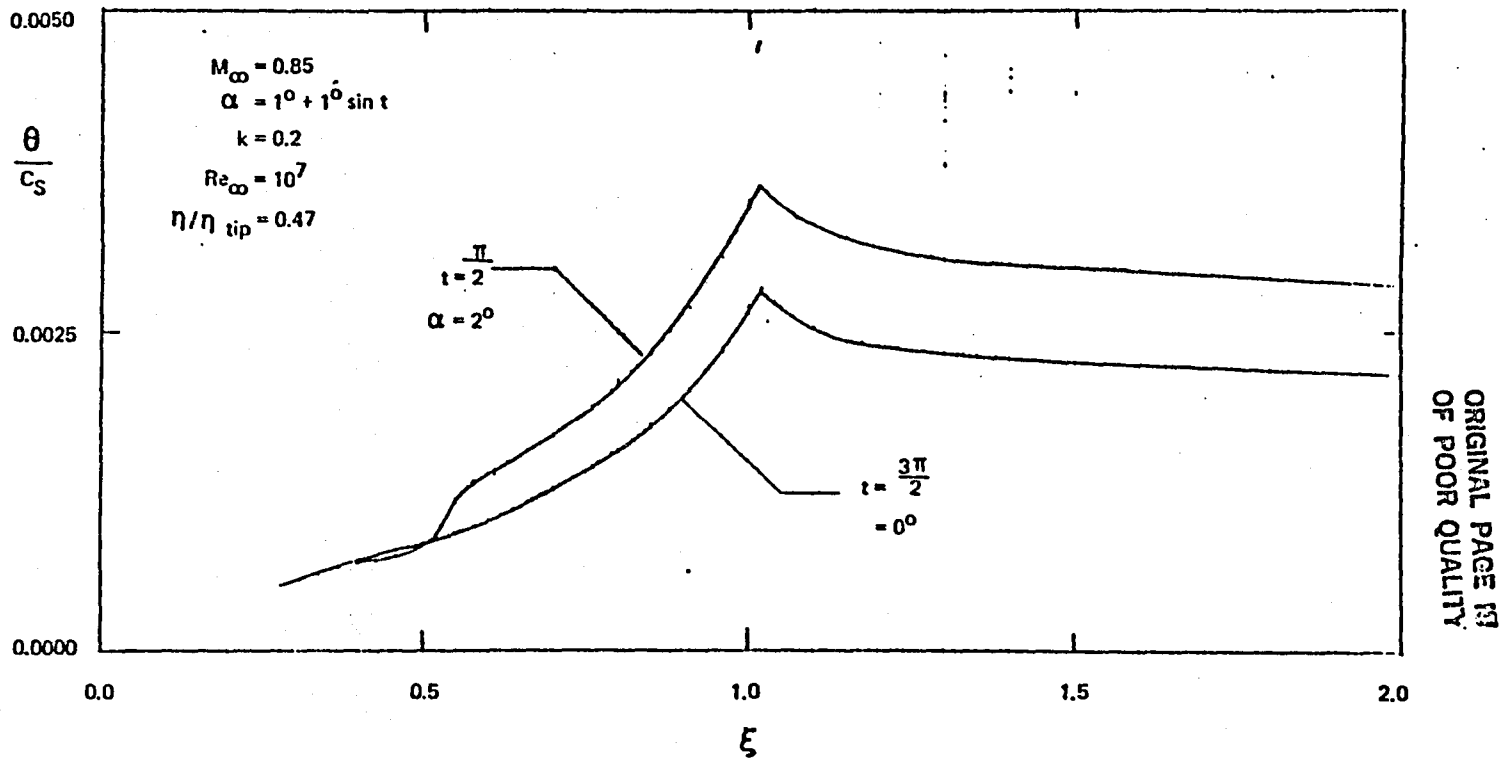

Figure 12. Unsteady Upper Surface Momentum Defect Thickness Distributions ofr MBB-A3 Wing at $\eta/\eta_{tip} = 0.47$

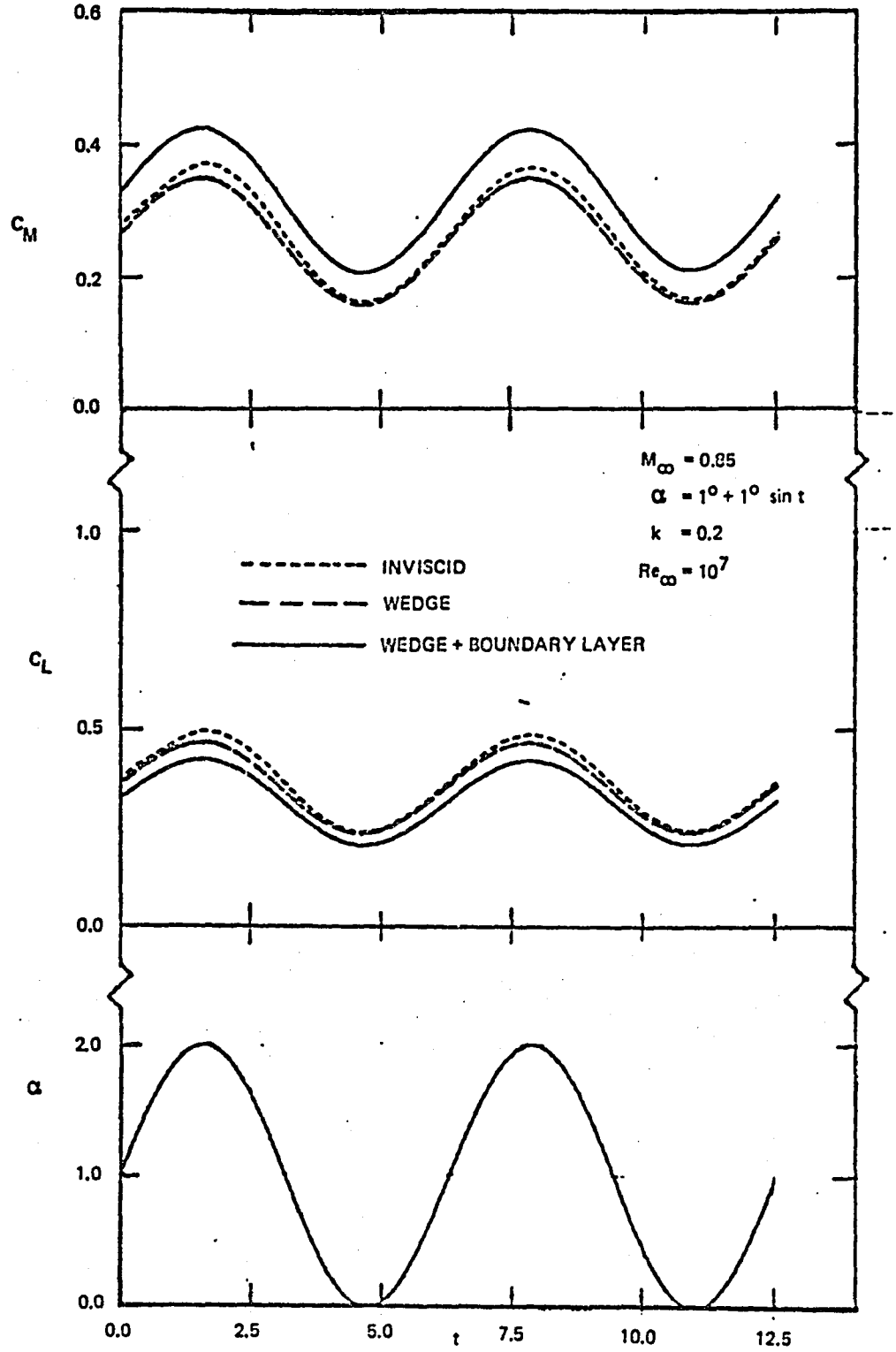

Figure 13. Unsteady Lift and Moment Coefficients for MBB-A3 Wing

END

DATE

FILMED

MAY 23 1984

End of Document